Highly-dispersed surface NiO species and exposed Ni (200) facets facilitating activation of furan ring for high-efficiency total hydrogenation of furfural

Qiuju Fu [a,b], Liting Yan [a,*], Dandan Liu [b], Shuo Zhang [b], Huimin Jiang [b], Wenpeng Xie [b], Lingzhi Yang [a], Yujia Wang [c], Haiyan Wang [c,*], Xuebo Zhao [a,b,**]

[a] School of Materials Science and Engineering, Qilu University of Technology (Shandong Academy of Sciences), Jinan 250353, PR China
[b] State Key Laboratory of Heavy Oil Processing, College of Chemistry and Chemical Engineering, China University of Petroleum (East China), Qingdao 266580, PR China
[c] School of Petrochemical Engineering, Liaoning Petrochemical University, Fushun 113001, PR China

ARTICLE INFO

ABSTRACT

Selective hydrogenation of biomass is indispensable to obtain high value-added chemicals. Herein, carbon-embedded Ni-based catalyst Ni/C-400 was prepared by employing a 3D flower-like MOF Ni-BDC as the sacrificial template. It featured highly exposed Ni (200) facets with abundant highly-dispersed surface NiO species, exhibited an outstanding catalytic performance toward the total hydrogenation of furfural (FFR), and achieved an exceptional tetrahydrofurfuryl alcohol (THFA) yield of 98.5 % under 80 °C and 1 MPa H_2. FFR/FFA-temperature program desorption (TPD) was designed for the first time to identify the adsorption capacity and strength between reactants and catalysts. Density functional theory (DFT) calculations confirmed that Ni particles with surface NiO species have a more substantial capacity to adsorb reactants, while the Ni (200) facets are capable of adsorbing more dissociated H atoms, which is the key to concurrently achieving high FFR conversion and THFA selectivity.

1. Introduction

Nowadays, propelled by global warming mitigation actions and ever-increasing energy demands, the production of high value-added chemical compounds and fuels from inexpensive and accessible biomass sources is garnering ever-increasing significance as a more environmentally friendly substitute for non-renewable crude oil. Furfural (FFR), obtained from the xylose through acid-catalyzed hydrolysis, is regarded as one of the "Top-10" platform molecules in biorefinery carbohydrates [1–3]. To date, FFR has been converted into many valuable chemicals and fuel additives such as furfuryl alcohol (FFA) [4], tetrahydrofurfuryl alcohol (THFA) [5], 2-methylfuran (2-MF) [6], furan [7] and so like (Scheme S1). As an essential precursor/environment-friendly solvent, THFA has been highly demanded in the industrial, agricultural, and automotive industries [8]. Thus, the selective hydrogenation of FFR to THFA in satisfying yields is undoubtedly of considerable practical significance and academic critical for FFR upgrading. However, the complicated pathways and harsh operation conditions still pose

significant challenges for rationally designing catalysts to obtain the target products with considerable yields.

Traditionally, THFA is produced by two-step hydrogenation of FFR via FFA as the intermediate under harsh conditions (140–180 °C, >4 MPa H_2) using commercially Cu-Cr catalyst and then noble metal catalysts [9]. To simplify the reaction process and increase atom availability, researchers have focused on developing highly efficient catalysts that can obtain THFA directly from FFR in one step. Many catalysts have been reported for one-step total hydrogenation of FFR, including noble and non-noble metal catalysts. Noble metals, such as Rh, Ru, Pd and Pt [10–13], possess remarkable catalytic activity and have been widely applied for the total hydrogenation of FFR. Although excellent performance has been achieved using precious metal-based catalysts, the high cost and scarce reserves have precluded their large-scale application. Many reports have shown that FFR preferably adopted a flat adsorption mode on the Ni surface, adsorbing and activating both furan ring and carbonyl groups for highly selective conversion to THFA [14,15]. Therefore, possessing the merits of high H_2 activation capability and low

* Corresponding authors.
** Corresponding author at: School of Materials Science and Engineering, Qilu University of Technology (Shandong Academy of Sciences), Jinan 250353, PR China.
E-mail addresses: yanlt@qlu.edu.cn (L. Yan), fswhy@126.com (H. Wang), zhaoxuebo@upc.edu.cn (X. Zhao).

price, Ni-based catalysts have garnered ever-increasing attention to substitute precious metal-based catalysts for total hydrogenation of FFR. Jadeja's group reported a series of bimetallic Ni-Co catalysts supported on SiC, γ-Al$_2$O$_3$, and SBA-15, of which 10 N-10 C-MS with smaller size and higher Ni-CoO$_x$ sites dispersion displayed the best catalytic activity with 90.4 % THFA selectivity at 210 °C and 7 MPa H$_2$ [16]. Wei et al. successfully synthesized two supported Ni catalysts (Ni/MMO-NO$_3$ and Ni/MMO-CO$_3$) with different exposed facets from NiAl-LDH precursors with NO$_3^-$ and CO$_3^{2-}$ as the interlayer anions [17]. Under 110 °C and 3 MPa H$_2$, Ni/MMO-NO$_3$ exhibited high selectivity toward FFA (97 %), while Ni/MMO-CO$_3$ showed good selectivity for THFA (99 %), confirming that the hydrogenation selectivity of FFR can be easily tuned by adjusting the exposed facets of Ni catalysts. Although research progress has been achieved, the harsh reaction conditions in THFA production may cause heavy infrastructural costs to a large degree. And the poor reusability of Ni-based catalysts owing to the deactivation at high reaction temperatures is not conducive to the effective hydrogenation reaction [15,18]. The mechanistic details on how catalyst structure (such as the degree of exposure and the exposed crystal facet of the active sites) can influence the adsorption configuration of FFR/FFA are still lacking. Besides, the reaction mechanism and the intrinsic active sites remain vague and ambiguous, which restricts the designing and preparing of efficient catalysts for catalyzing FFR to THFA [19]. Therefore, a deeper exploration and more characterizations for elucidating the adsorption behavior between reactants (FFR/FFA/H$_2$) and catalytic active sites is necessary to further reveal the reaction mechanism.

Metal-organic frameworks (MOFs) [20,21], self-assembled from inorganic metal ions or clusters and organic linkers, have evoked much attention in the academic field due to their unique properties such as high surface area, tunable pore structure, and easy functionalization, which have been extensively used for developing carbon-based nanomaterials, metal-based compounds and their hybrids [22,23]. MOF-derived porous metal/carbon (M/C) materials have made extraordinary contributions in many fields, especially in catalytic hydrogenation. Zhao's group successfully synthesized Fe-Co nanoparticles on N-doped carbon supports using ZIF-67 as a precursor and achieved high performance in the selective hydrogenation of cinnamaldehyde to cinnamyl alcohol [24]. Zou et al. modulated the synthesis of polymetallic-doped ZIF-derived materials for the efficient hydrogenation of FFR to FFA through a homogeneous doping and self-templating strategy [25]. Tang et al. reported a Ni-Cu alloy catalyst by employing NiCu$_x$-BTC as a sacrificial template and used it for the total hydrogenation of FFR [26]. Good performance was obtained over the NiCu$_{0.33}$/C catalyst at 150 °C, 3 MPa H$_2$ pressure and 18 h. Compared to 3D M/C materials, 2D M/C materials has noticeable advantages. For one thing, the ultra-nanosheets of 2D MOFs make it possible to stabilize metal particles with a homogeneous distribution [27]. For another, the nanocomposites obtained from 2D MOFs could drastically increase the exposure of active sites to catalyze the target reactions efficiently. Zhu group synthesized 3D, 2D, and bulk MOF-FeCo by simply adjusting the solvent and concluded that 2D-MOF performed better activity owing to more exposed active sites [28]. Therefore, 3D ordered structures assembled by interconnected 2D nanosheets with porous structures inherit not only the exceptional advantages of the 2D structure but also prevent the stacking of 2D nanosheets [29], which is incredibly desirable for catalytic reactions [30].

Herein, we prepared carbon-embedded Ni-based catalysts treated under different temperatures (denoted as Ni/C-T, where T stands for pyrolysis temperature) by employing a 3D flower-like MOF Ni-BDC self-assembled by 2D nanosheets as a sacrificial template. The 2D ultrathin Ni-BDC nanosheets can constrain the size of Ni particles and ensure highly exposure of the Ni particles for better catalytic reactions. The results showed that the distribution of surface NiO species and exposed facets of Ni nanoparticles were successfully modulated by adjusting the heat treatment temperature. Notably, the Ni/C-400 sample showed a

high yield of THFA (98.5 %) under moderate conditions. Abundant surface NiO species were confirmed in the Ni/C-400 sample by XPS and XAS tests, which is demonstrated to be highly related to the catalytic activity. FFR/FFA-temperature program desorption (TPD) tests was designed for the first time, and the results indicated that the Ni/C-400 sample has a strong adsorption interaction with reactants, which laid the foundation for exploring the reaction mechanism. Theoretical calculations showed that the d-band center of Ni (200) facet displayed upshift energy than that of Ni (111) facet, which enhances the adsorption interaction between FFR/FFA/H$_2$ molecules and active sites. Meanwhile, Ni (200) facets were proven to facilitate the formation of dissociated H atoms, endowing the Ni/C-400 sample with remarkable activity. The controlled adjustment of Ni particles microstructure has extremely remarkable influence on the adsorption capacity of reactants, which determines the reactivity of the hydrogenation.

2. Experimental procedures

2.1. Synthesis of Ni-BDC

Ni-BDC nanoparticles were obtained by a previous report with some modification [31]. Typically, 0.3565 g (1.5 mmol) portion of NiCl$_2$ 6 H$_2$O and 0.2492 g (1.5 mmol) portion of 1, 4-terephthalic acid (H$_2$BDC) were dissolved into a mixture solvent of N, N-dimethylformamide (DMF), H$_2$O, ethanol (36 mL, V: V: V=16: 1: 1). After stirring, the solution was sealed and treated at 120 °C for 48 h. After cooling to room temperature, the products were filtered and washed three times with ethanol, and then dried at 80 °C overnight to collect the Ni-BDC products (yield: 80.4 %).

2.2. Synthesis of Ni/C-T samples

In a typical procedure, Ni-BDC was placed in the center of ceramic boats under continuous high-purity N$_2$ flow. The boat was heated at a specific temperature for 3 h (5 °C·min^{-1}). The remained black nanoflower powder were collected. The obtained samples were denoted as Ni/C-T (T = 400, 500, and 600), where 400, 500, 600 represent the target temperature (400, 500, 600 °C), respectively. Before taking the samples out of the tube furnace, N$_2$ was used as a protective atmosphere to encapsulate the catalyst in a nitrogen-filled sample tube for storage. Before the characterization and catalytic reaction, the catalyst was immediately taken out for subsequent testing.

2.3. Catalytic evaluation

The hydrogenation of FFR is performed in a 100 mL stainless steel autoclave (Beijing Century Senlong, SML-100). Typically, 0.6 g of FFR, 0.1 g catalyst, and 50 mL of ethanol are poured into the autoclave. After the reactor was sealed, the reaction system was purged with hydrogen gas three times to exclude air and then filled it with specific hydrogen H$_2$ pressure. The stirring speed was set at 800 rpm. After the reaction, the liquid products were analyzed by a gas chromatograph. The conversion of FFR (C_{FFR}) and the selectivity of THFA (Y_{THFA}), FFA (Y_{FFA}) and byproducts ($Y_{byproducts}$) are calculated using the formulae as follows.

$$C_{FFR} = \frac{n_{FFR,\,0} - n_{FFR,\,t}}{n_{FFR,\,0}} \times 100\% \tag{1}$$

$$Y_{FFA} = \frac{n_{FFA,\,t}}{n_{FFR,\,0} - n_{FFR,\,t}} \times 100\% \tag{2}$$

$$Y_{THFA} = \frac{n_{THFA,\,t}}{n_{FFR,\,0} - n_{FFR,\,t}} \times 100\% \tag{3}$$

$$Y_{byproducts} = 1 - Y_{FFA} - Y_{THFA} \tag{4}$$

In which $n_{FFR,\,0}$ is the initial mole of FFR before reaction, $n_{FFR,\,t}$ is the

mole of FFR in the reaction, $n_{FFA, t}$ represents the mole of FFA in the reaction, $n_{THFA, t}$ represents the mole of THFA in the reaction.

2.4. Catalyst characterization

X-ray diffraction (XRD) patterns were measured on a Panalytical X´Pert PRO MPD X-ray diffractometer. Transmission electron microscopy (TEM) and high-resolution transmission electron microscopy (HRTEM) were conducted by a FEI TECNAI G2 F20 instrument conducting at 200 kV. The morphology of products was studied by using a ZEISS Sigma300 field-emission scanning electron microscopy (SEM) microscope. Thermal gravimetric analysis (TGA) data were obtained on a PerkinElmer TGA 8000 thermogravimetric analyzer with a heating rate of 10 °C·min^{-1} in N$_2$ atmosphere. The structural properties of the samples were collected by nitrogen physical adsorption at 77 K on a Quantachrome Autosorb-iQ apparatus. Before measurement, the Ni-BDC samples and the carbonized samples were activated for 12 h under vacuum at 100 °C and 200 °C, respectively. Gases generated from the heating treatment process of Ni-BDC were measured by mass spectrometry (MS) (Hiden HPR-20). The pore size distribution was calculated from the desorption branch using the nonlocal density functional theory (NLDFT) method. X-ray photoelectron spectra (XPS) were obtained using an X-ray photoelectron spectrometer (ThermoFisher, ESCALAB 250Xi). The measure XPS energies were corrected at 284.8 eV using the C1s peak of the C-C bond. The qualitative analysis of liquid products was performed by GC-MS Thermo (ISQ LT) trace instrument. Raman spectrum was recorded using Horiba Scientific LabRAM HR Evolution, with a laser excitation wavelength of 633 nm. The X-ray absorption near edge structure (XANES) measurement of Ni/C-400 was performed at Singapore Synchrotron Light Source, facility for catalysis research (XAFCA) beamline. UPS He II spectra were acquired using a ThermoFisher (ESCALAB Xi+) in ultrahigh vacuum conditions. The binding energy scale was calibrated by measuring the Fermi level of an Au sample. Atomic force microscopy (AFM) images were measured using a Bruker (Dimension ICON) probe microscope. Inductively Coupled Plasma-Optical Emission Spectrometer (ICP-OES, Agilent 5110) was used to obtain elemental analysis.

The hydrogen adsorption capacity and reduction behavior of the samples were conducted by a Builder PCA-1200 TPD/TPR instrument with a thermal conductivity detector (TCD). In the program of H$_2$-TPD, the sample (70 mg) was sealed in a quartz tube, followed by activating at 250 °C for 100 min under a gas mixture of H$_2$/Ar (1: 9, V/V) to remove water and solvents trapped in the channels before hydrogen adsorption. Then, under the protection of the above-mentioned mixture gas, the sample was cooled to 80 °C and exposed at 80 °C for 40 min to ensure that the metal surface was saturated by H$_2$ (30 mL·min^{-1}). Subsequently, the samples were slowly purged under Ar (30 mL·min^{-1}). After the baseline is stabilized, the sample is heated to 400 °C at a rate of 10 °C·min^{-1}. In this process, the desorption signal of hydrogen is detected by TCD. In the program of H$_2$-TPR, the samples (50 mg) were first activated at 300 °C (100 °C for Ni-BDC) under Ar for 60 min to remove water and other adsorbates. Next, the samples were cooled to room temperature and then heated under H$_2$/Ar (1: 9, V/V, 30 mL·min^{-1}) from room temperature to 800 °C (10 °C·min^{-1}). In this process, the Ni/C-T catalysts is gradually reduced by reacting with hydrogen during the heating process, and the depletion signal of hydrogen is detected by TCD.

The FFR and FFA chemisorbed capacity of the catalysts were also conducted with a Builder PCA-2200 TPD/TPR instrument. In the program of FFR-TPD, the catalyst (20 mg) mixed with 20 μL pure FFR was sealed in a quartz tube, followed by activating at 150 °C for 120 min under Ar (30 mL·min^{-1}) to remove physical adsorbed FFR molecules trapped in the channels. After the baseline is stabilized, the sample is heated to 400 °C under He (30 mL·min^{-1}) at a rate of 5 °C·min^{-1}. In this process, the desorption signal of FFR is detected by TCD. The procedure of FFA-TPD was identical to that of FFR-TPD, except that FFA is substituted for FFR.

The in-situ FT-IR of FFR absorption was measured using a Nicole iS50 infrared spectrometer. The sample was treated by helium (100 mL·min^{-1}) at 200 °C for 60 min, and then cooled to room temperature. Subsequently, FFR was introduced into the cell for 30 min, and then followed by flowing helium (100 mL·min^{-1}) for another 30 min. After H$_2$ (30 mL·min^{-1}) was introduced into the cell, heating began, FT-IR spectra then were recorded at 30 °C, 40 °C, 50 °C, 60 °C, 70 °C and 80 °C, respectively. The control test was conducted by replacing the sample with commercially purchased γ-Al$_2$O$_3$.

2.5. Computational details

The calculations was performed with the density function theory (DFT) method, using the Vienna ab initio simulation package (VASP) [32,33]. The projector augmented wave (PAW) method and the generalized gradient approximation (GGA) with the Perdew-Burke-Ernzerhoff (PBE) functional were used to solve the Kohn-Sham equations. The slab models of pure Ni and Ni/NiO (Ni surface with a NiO cluster) as well as Ni (111) and Ni (200) were constructed, respectively. DFT calculations were conducted with a cutoff energy of 400 eV and 4 × 4 × 1 k-point Monkhorst-Pack grid. The convergence criteria for the electronic self-consistent iteration and force were set to 10^{-4} eV and 0.05 eV Å^{-1}, respectively.

The adsorption energies (E$_{ads}$) of the reacted molecules were obtained based on the following equation:

$$E_{ads} = E_{total} - (E_{surface} + E_{molecule})$$

Where, E$_{total}$ is the total energy of the catalyst surface with the absorbed reacted molecules, E$_{surface}$ is the energy of selected metal surface, E$_{molecule}$ is the energy of free molecules.

3. Results and discussion

3.1. Synthesis and characterizations of Ni/C-T catalysts

Fig. 1a schematically illustrates the simple solvothermal-pyrolysis strategy for preparing 3D flower-shaped Ni/C-T samples. Briefly, nickel salts, H$_2$BDC and solvents were mixed in the autoclave at 120 °C for 48 h to obtain Ni-BDC samples [34]. 3D flower-shaped Ni-BDC precursors with uniform morphology and high crystallinity were used as a template for the preparation of Ni/C-T catalysts. The powder X-ray diffraction (XRD) pattern of the as-prepared Ni-BDC matches well with the simulated crystal structure, confirming the successful synthesis of Ni-BDC [35] (Fig. 1b). N$_2$ adsorption-desorption measurement was conducted to study the pore channel information of the as-synthesized Ni-BDC. As displayed in Fig. 1c, the Ni-BDC sample exhibited type IV isotherms with a giant hysteresis loop. The specific surface area of Ni-BDC measured using the Brunauer-Emmett-Teller is 74 m^2·g^{-1}, all of which belongs to the existence of mesopores. Meantime, Ni-BDC has a main pore size centered at 5 nm (Fig. 1d). The mesopores in Ni-BDC may be ascribed to the intercalation of 2D nanosheets, which facilitates the exposure of active sites.

The thermal stability of Ni-BDC was explored to determine the appropriate carbonization temperature using thermogravimetric (TG) analysis. The framework of Ni-BDC began to collapse at approximately 380 °C (Fig. S1). Besides, samples achieved by treating Ni-BDC at 300 °C and 350 °C presented the same XRD pattern as the precursor (Fig. S2). Therefore, 400 °C was chosen as the starting annealing temperature to convert Ni-BDC in-situ into supported Ni-based materials. It was apparent that the characteristic peaks of Ni-BDC disappeared, implying the complete decomposition of the precursor framework after annealing at 400 °C for 3 h (Fig. 1e). In the XRD patterns of the Ni/C-T samples, three diffraction peaks at 44.5°, 51.8° and 76.4° can be assigned to the (111), (200) and (220) crystal planes of the face-centered cubic (fcc)
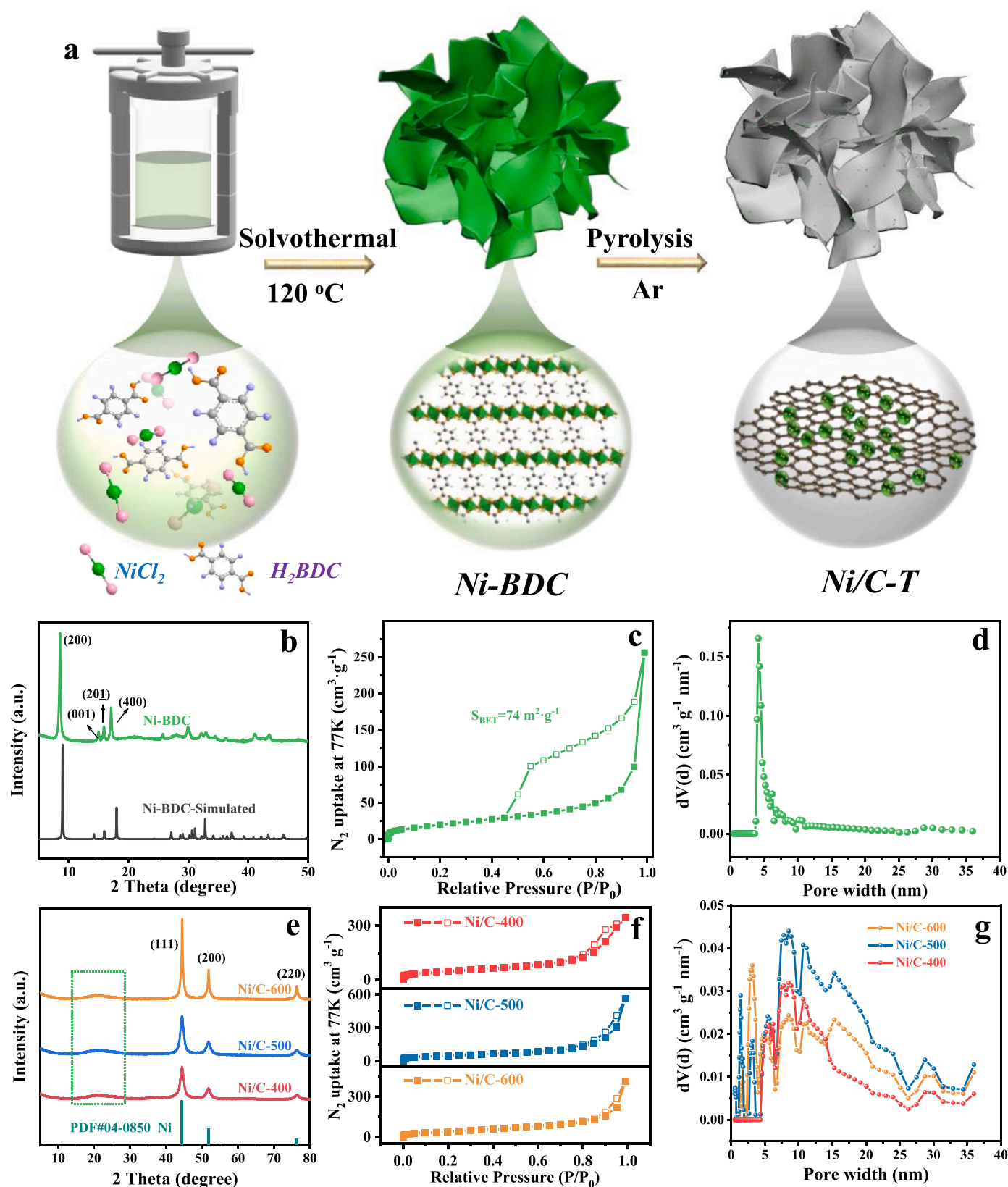
Fig. 1. a) Schematic of the preparation of Ni-BDC and Ni/C-T, b) XRD pattern of Ni-BDC, c) N₂ adsorption-desorption isotherm of Ni-BDC, d) pore size distribution of Ni-BDC, e) XRD patterns of Ni/C-T samples, f) N₂ adsorption-desorption isotherms of Ni/C-T at 77 K and g) pore size distribution of Ni/C-T samples (Calculated by the nonlocal density functional theory (NLDFT) model).

phase of Ni (JCPDS card no. 04-0850), respectively (Fig. 1e). N_2 physisorption measurement showed that the carbonized samples all have a wide range of mesoporous distribution, and higher specific surface area than Ni-BDC (Fig. 1f, g and Table S1). It is worth noting that the Ni/C-400 sample with a high specific surface area of 170 $m^2 \cdot g^{-1}$ contains only mesopores, while the Ni/C-500 and Ni/C-600 samples are micro-mesoporous materials. The increased specific surface area of the Ni/C-T samples can attributed to the generation of numerous nanoparticles during the carbonization process resulting in the formation of abundant porous structure [36]. Normally, abundant mesoporous channels can efficiently facilitate the transportation of substrate molecules (especially for FFR/FFA molecules) and contribute to high catalytic activity [37]. The Raman analysis was carried out to explore the graphitization degree of Ni/C-T catalysts, indicating the existence of predominately amorphous carbon (Fig. S3).

The morphology of the 3D Ni-BDC nanoflowers is depicted in Fig. 2 and Fig. S4. SEM images revealed that 3D Ni-BDC particles display a relatively uniform distribution with a diameter of about 5–6 μm. This porous 3D flower-like structure consists of cross-linked porous 2D nanosheets with a relatively smooth surface (Fig. 2a). Moreover, these sheets are interconnected in different orientations with clear open spaces between adjacent nanosheets. Curved and crinkled morphology of the edges of the 2D nanosheets is observed in the enlarged SEM images due to the ultra-thin and large size of the 2D nanosheets (Fig. 2b). The thickness of the nanosheets in 3D Ni-BDC was characterized by atomic force microscopy (AFM) and measured to be 2.5–3.5 nm (Fig. 2c and Fig. S5). The low contrast at the edge and visible dark parts caused by folded of the sheets also prove the presence of ultrathin nanosheets (Fig. 2d-e). Besides, the ultrathin properties of 2D nanosheets in Ni-BDC

were confirmed by light scattering experiments. The Tyndall effect of ultrathin 2D nanosheets in Ni-BDC was observed in the colloid suspension in water (Fig. S6). Furthermore, a high-resolution TEM (HRTEM) was carried out to disclose the crystal structure information from Ni-BDC. An interplanar spacing of 1.04 nm can be observed, which belongs to the lattice fringes of the (200) planes of Ni-BDC (Fig. 2 f). Moreover, the corresponding FFT image substantiates its single crystalline nature.

Fig. 3 displays the TEM and SEM images of the Ni/C-T samples, and it is obvious that they perfectly inherit the 3D flower-like morphology of the precursor. It can be concluded that the carbonization process does not cause remarkable effects on the appearance of the Ni/C-T samples, except for the roughened surface of the nanosheets. Significantly, it was speculated that these 3D unique structures optimize the hydrogenation performance by providing effective reaction substrate/hydrogen contacts throughout the whole reaction system and ensuring the adequate exposure of active sites available for the catalytic hydrogenation reactions. As can be seen from the TEM results, the average size of Ni nanoparticles in Ni/C-400, Ni/C-500 and Ni/C-600 was calculated to be 6.39 nm, 6.89 nm and 7.46 nm, respectively (Fig. 3a_2-c_2). The tiny metallic Ni nanoparticles were homogenously embedded or constrained in the ultrathin 2D porous carbon matrix. With increasing temperature, these Ni nanoparticles showed negligible aggregation (<1 nm), originating from the confinement effect of ultrathin 2D nanosheets. In addition, SEM images also demonstrated that the distribution and size of the Ni nanoparticles appeared to be insignificant aggrandizement as the carbonization temperature increased (Fig. 3a_4-c_4), which is consistent with the TEM results. Besides, the thickness of the nanosheets in the Ni/C-T samples was measured to be 3–4 nm, demonstrating that the heat
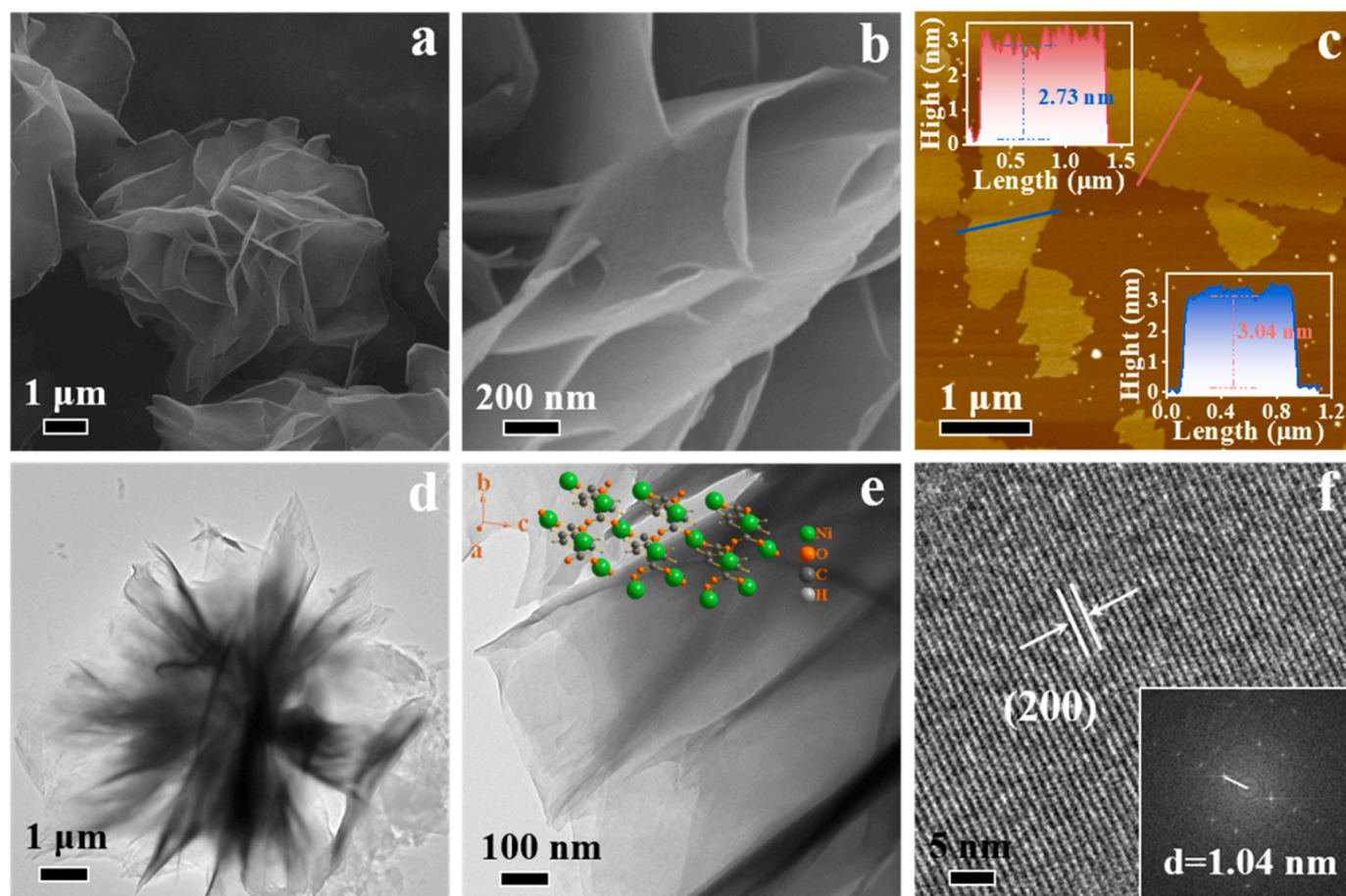

Fig. 2. a, b) SEM images of Ni-BDC. c) AFM image and corresponding height profiles of Ni-BDC nanosheets along the red and blue lines, respectively. d, e) TEM images of Ni-BDC, Inset in (e): the corresponding crystal structure of Ni-BDC in the (200) plane. f) HRTEM and FFT images of Ni-BDC.
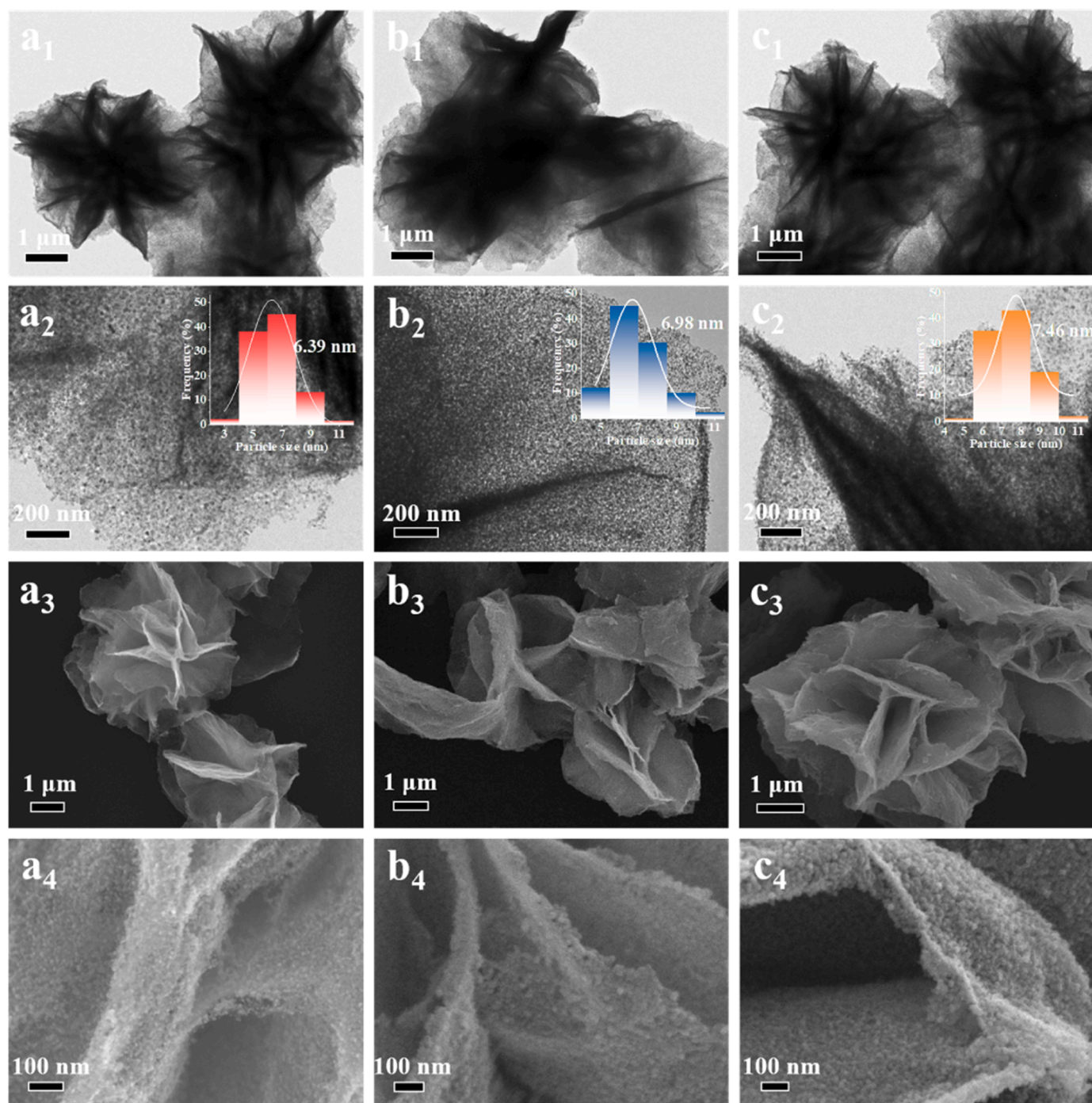
Fig. 3. Electron microscope images of a) Ni/C-400, b) Ni/C-500, c) Ni/C-600. Line 1: TEM images, Line 2: TEM images and corresponding particle size distribution profile, Line 3–4: SEM images with different magnifications.

treatment process did not destroy the ultrathin properties of the nanosheets (Fig. S7-9). With such ultrathin support, it is reasonable to speculate that the metal particles in the Ni/C-T sample are embedded in the carbon support, which ensures the exposure of as many metal active sites as possible to effectively catalyze the hydrogenation reaction.

The X-ray photoelectron spectroscopy (XPS) survey of Ni/C-T samples reveals the existence of Ni, C, and O elements (Fig. 4a). From the XPS spectra, the Ni atom content exhibits an increasing trend while the content of the O atom presented an opposite trend with increasing carbonization temperatures (see the XPS in Fig. 4a and Table S2). The higher O content in the Ni/C-400 suggests that the O atoms in the ligand are partially retained at this temperature. CO_2, CO, H_2, CH_4 generated

from the decomposition of Ni-BDC framework are monitored by mass spectrometry (MS). There is no doubt that significant amounts of O atoms are still preserved in the framework under 400 °C since only modest amounts of CO_2 and CO escaped (Fig. S10-11). From the high-resolution O 1 s spectra, three peaks centered at 530 eV, 531.9 eV and 533.7 eV can be assigned to the oxygen atoms in the lattice oxygen in Ni-O, C=O and O-H groups, respectively (Fig. 4b) [36,38]. The relative area of the Ni-O peak obviously decreased with the carbonization temperature increase, confirming the decrease in the Ni-O content (Table S3). Besides, the high-resolution XPS spectrum of C 1 s displayed three significant peaks at 284.8 eV, 286 eV and 289 eV, which correspond to carbon atom bonds: C-C, C-O and O=C-O, respectively (Fig. 4c)
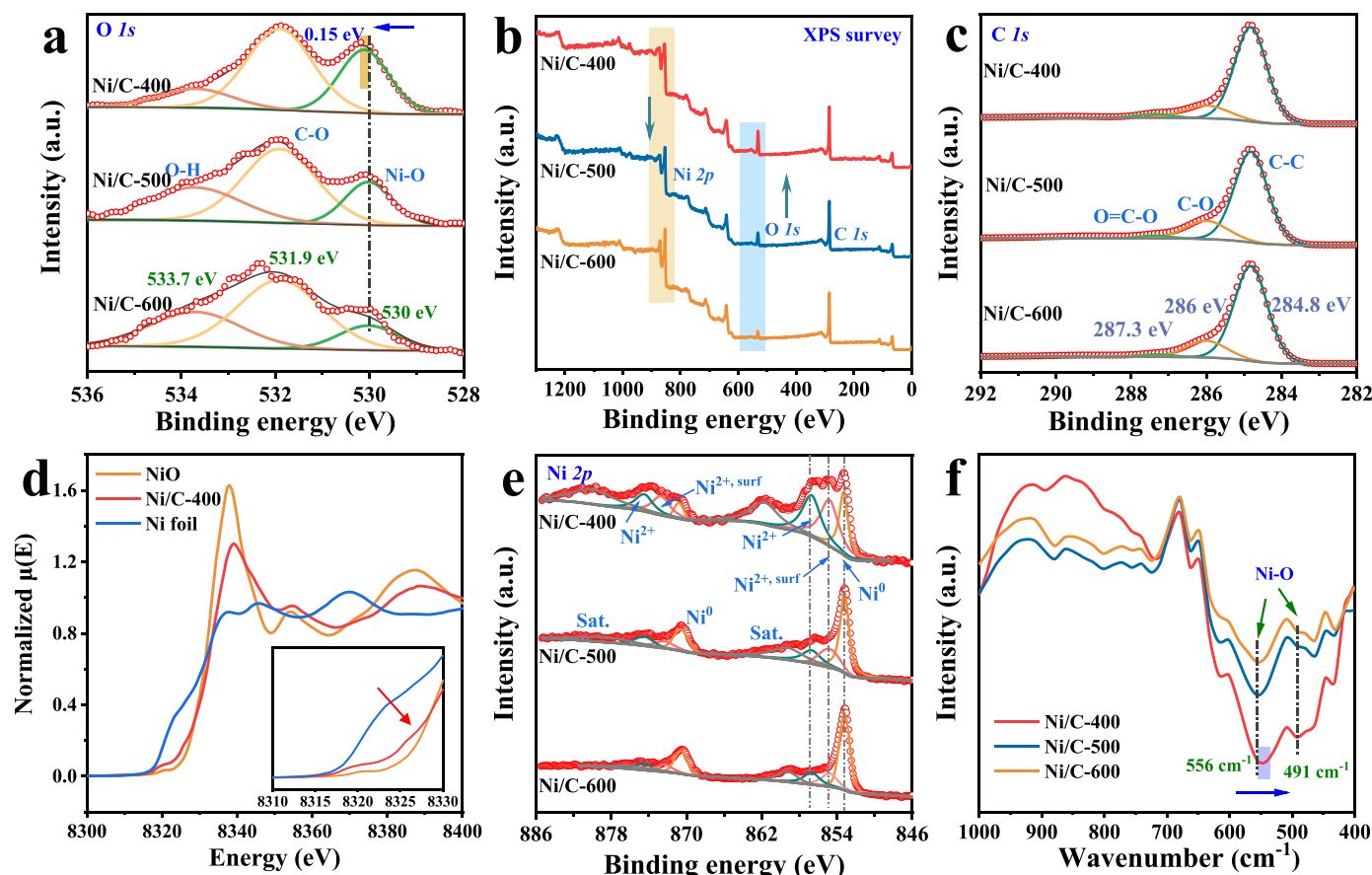
Fig. 4. a) XPS surface profiles, b) O 1 s XPS spectra, c) C 1 s XPS spectra of Ni/C-T samples. d) Ni K-edge XANES spectra of the Ni/C-400 and reference samples (NiO and standard Ni foil). e) Ni 2p XPS spectra of Ni/C-T samples, f) FT-IR spectra of Ni/C-T samples.

[24]. The high content of Ni-O peaks and O atoms in the Ni/C-400 sample motivated us to hypothesize that it contains considerable portions of highly-dispersed and non-well-crystallized NiO species that cannot be detected by XRD (Fig. S12). To validate this hypothesis, X-ray absorption near-edge structure (XANES) and extended X-ray absorption fine structure (EXAFS) were further analyzed. As shown in Fig. 4d, the Ni K-edge XANES spectrum of Ni/C-400 is located between NiO and Ni foil, reflecting that the valence of the Ni species is between 0 and 2 [39]. Moreover, the EXAFS spectrum and wavelet transform (WT) results of Ni/C-400 demonstrated partial Ni existed in the form of NiO species (Fig. S13-15). From the SEM-mapping of the Ni/C-400 sample, C, O and Ni elements were homogeneously distributed over the Ni/C-400 sample (Fig. S16). The distribution of the O element was perfectly matched with the Ni element, implying that O species exist in the form of NiO. Two typical peaks are found at 853.3 eV and 870.8 eV in the Ni 2p spectra, corresponding to Ni metal species (Fig. 4e) [36]. Moreover, two characteristic peaks centered at 856.7 eV and 874.5 eV can be attributed to Ni^{2+} (bulk NiO) peaks. S. Palacín et al. have experimentally and theoretically investigated the surface effects of NiO and demonstrated that the surface Ni atoms display lower binding energies than bulk Ni atoms in NiO [40]. They found that NiO is composed of surface Ni atoms (NiO_5 in pyramidal) and bulk Ni atoms (NiO_6 in octahedral), indicating the existence of O defects in the surface NiO species [40]. Therefore, two peaks centered at 854.8 eV and 872.7 eV, located in the middle of Ni^0 and Ni^{2+} peaks, which could be assigned to the above-mentioned surface NiO species (denoted as $Ni^{2+, surf}$) [40,41]. The presence of O defects in the surface of NiO compared to the bulk NiO species endows the exposure of abundant surface Ni^{2+} sites, affording tremendous opportunities for catalytic reactions. Besides, commercial nanosized NiO was purchased to confirm the existence of surface Ni^{2+} species in Ni/C-T

samples (Fig. S17-18). According to the XPS peak, the content of total Ni^{2+} in the Ni/C-400 sample is as high as 76.45 %, which is in accordance with the EXAFS results (Fig. S19 and Table S4). Furthermore, the contents of total Ni^{2+} decreased to 45.43 % and 42.34 % in Ni/C-500 and Ni/C-600 samples, respectively. Hence, it also confirmed that the surface NiO species in NiC-T samples were not caused by the exposure of the samples to air, as the Ni^{2+} content differed greatly in the samples. The change of Ni species verifies the transition from Ni atoms in Ni-BDC to Ni particles with highly-dispersed surface NiO species, and then to pure metallic Ni with increasing annealing temperature. Therefore, the Ni/C-400 sample is a transition state between the Ni-BDC precursor and the completely pyrolyzed sample.

From the FT-IR spectra, two intense peaks at 491 cm^{-1} and 556 cm^{-1} confirm the appearance of metal-oxygen stretching vibration of Ni-O in the Ni/C-T samples, and the peak intensity in the Ni/C-400 sample is significantly higher than the other samples [42] (Fig. 4f). Moreover, it was noteworthy that an apparent redshift phenomenon appeared in the peak located at 556 cm^{-1} in the Ni/C-400 sample, which confirms the presence of abundant highly-dispersed surface NiO species. In contrast, the disappearance of the redshift phenomenon in the Ni/C-500 and Ni/C-600 samples indicated the absence of surface NiO species. And the broad absorption peak located at 3450 cm^{-1} corresponds to the stretching vibration mode of the hydroxyl group, as obtained due to the absorption of water molecules on the surface of the Ni/C-T sample (Fig. S20). Herein, calcination at different temperatures reflected to the in-situ structural evolution of the Ni-BDC framework, manipulating the existing forms of Ni species.

3.2. Catalytic performance toward total hydrogenation of FFR

It is well recognized that Ni-based catalysts are widely used in FFR hydrogenation catalytic reactions due to their high activity [16,43]. The selective hydrogenation of FFR could occur on the extra-ring C=O or both furan ring and C=O, leading to the formation of FFA or THFA, respectively. The latter conversion pathway is thermodynamically preferable but more challenging due to the highly stable properties of the furan ring [44]. To study the catalytic performance of the as-prepared Ni-based catalysts, the hydrogenation studies were performed for the FFR reaction (Table 1). FFR hydrogenation reactions were carried out in ethanol at 70 °C and an initial H_2 pressure of 1 MPa. In the absence of a catalyst, the FFR can react with ethanol to obtain 3.7 % conversion of 2-(diethoxymethyl)furans (2-DEMF) under reaction conditions (Fig. S21), and there are no hydrogenation products generated (Table 1, Entry 1). Moreover, Ni-BDC was catalytically inactive for the THFA formation (Table 1, Entry 2), which can be attributed to the lack of active catalytic sites in the MOF framework for the hydrogenation of FFR. Hence, the periodically arranged Ni^{2+} species (Ni-O nodes) in Ni-BDC were incapable of activating hydrogen. To better compare the catalytic activity of the as-prepared Ni-based catalysts, commercially purchased Ni powder was selected as the catalyst for the FFR hydrogenation reaction (Fig. S22). The results revealed that Ni powder had relatively poor FFR hydrogenation reactivity and could not obtain THFA products under setting conditions, which may be due to the large Ni particle sizes and the insufficient number of exposed Ni sites (Table 1, Entry 3). Besides, NiO-400 derived from Ni-BDC heat-treated under air conditions could not catalyze the hydrogenation route of FFR, indicating that pure NiO species fail to activate hydrogen (Fig. S23 and Table 1, Entry 4). Impressively, the reaction performed with the Ni/C-400 catalyst displayed remarkable catalytic performance with 99.7 % conversion of FFR and 85.4 % selectivity to THFA after 4 h (Table 1, Entry 5). By comparing with precursors with thicker 2D nanosheets, we also confirmed that the 2D ultrathin nanosheet-derived catalysts can expose more catalytic active sites and thus feature higher catalytic activity (Fig. S24-28, Table S5-S6). Besides, it was shown that prolonging the heat treatment time reduces the exposure of metal active sites, leading to poorer catalytic performance (Fig. S29-30, Table S7). The FFR conversion and distribution of products were greatly influenced by the pyrolysis temperature: the conversion of FFR decreased to 91.5 % and the selectivity of THFA rapidly decreased to 40 % over Ni/C-500 catalyst (Table 1, Entry 6). Surprisingly, the activity and product distribution of the Ni/C-600 catalyst deteriorated considerably as the pyrolysis temperature was increased to 600 °C, with only 4.3 % THFA selectivity under lower FFR conversion (36.8 %) (Table 1, Entry 7). Despite the high content of Ni metal in Ni/C-600, the performance is not favorable, implying that surface NiO species play an overwhelming role in the hydrogenation process.

Table 1
The catalytic performance of different catalysts.

Entry	Catalysts	Conversion (%)	Selectivity (%)			
			FFA	THFA	2-DEMF	Others
1	None	3.7	0	0	100	0
2	Ni-BDC	2.3	0	0	100	0
3[a]	Ni powder (commercial)	29.9	3.3	0	80.8	15.9
4	NiO-400	17.1	0	0	100	0
5	Ni/C-400	99.7	14.5	85.4	0.1	0
6	Ni/C-500	91.5	58	40	1.9	0.1
7	Ni/C-600	36.8	19.4	4.3	75.4	0.9
8[b]	Ni/C-400	99.8	5.9	94	0.1	0

Reaction conditions: 0.6 g FFR; 0.1 g catalysts; 50 mL of ethanol; 70 °C; 1 MPa initial H_2 Pressure; 4 h. [a]80 °C; [b]80 °C, 0.5 MPa H_2 Pressure: additional H_2 is added to maintain constant pressure during the reaction process.

Furthermore, the kinetic studies of the FFR hydrogenation were also conducted on Ni/C-T samples over the temperature range 323–363 K. Since the Ni/C-T samples possess unique 3D flower-like morphology and the reaction proceeded at a high reaction speed, we can reasonably assume that the internal and external diffusion have almost no influence on the kinetic study. The apparent activation energy (E_a) of FFR hydrogenation was calculated according to the Arrhenius equation (Fig. 5). The plots of -ln (1-X) versus time (where X represents the conversion of FFR) obtained from the FFR conversion-time spectrum are straight lines, indicating that the FFR hydrogenation reaction is a pseudo-first-order reaction (Fig. 5a-c and Fig. S31-33). Depending on the results of the first-order kinetic fitting curve, the Arrhenius plot is roughly obtained, and the apparent activation energy is calculated based on the Arrhenius equation. The E_a value for FFR hydrogenation over Ni/C-400 (35.8 kJ·mol^{-1}) is much smaller than that over Ni/C-500 (60.3 kJ·mol^{-1}) and Ni/C-600 (81.4 kJ·mol^{-1}) (Fig. 5d-f), which indicates that the energy for FFR activation over Ni/C-400 can be considerably reduced. The low E_a value in Ni/C-400 should be correlated closely with its special active sites, rendering it an extremely high catalytic activity. Besides, the E_a value is significantly lower than those reported for Ni-based or even noble-based catalysts [45,46], which is the reason why the Ni/C-400 catalyst exhibits an unusual activity even at low H_2 pressure.

3.3. H_2/FFR/FFA-temperature program desorption (TPD) analysis

H_2-TPD (temperature-programmed desorption) measurement was conducted to explore the adsorption of hydrogen on Ni/C-T samples (Fig. 6a). Hydrogen is reported to dissociate on the surface of metallic Ni, which can be used to identify different modes of chemisorption and the number of each mode [47]. The position of desorption peaks reflects the strength of the interaction between Ni species and hydrogen. It has been reported that the hydrogen desorption peak appearing below 200 °C is ascribed to the bridge adsorption at Ni-Ni coordination [48], which reflects the relatively weak chemosorbed hydrogen [49]. In general, the area of the desorption peak reflects the amount of chemisorbed hydrogen, which indicates the number of active Ni sites. The desorption area decreases with increasing the annealing temperature, demonstrating that the Ni/C-400 sample possesses the highest contents of active Ni sites. The corresponding temperatures of the desorption peak centers of Ni/C-400, Ni/C-500 and Ni/C-600 are around 198 °C, 179 °C and 171 °C, respectively, which also implies that the interaction between hydrogen and Ni sites weakens with the increase of carbonization temperature. Notably, a new desorption peak centered at 378 °C appeared in the Ni/C-400 sample, which did not occur in the other samples. This new peak can be attributed to the aforementioned highly-dispersed surface NiO species, which belongs to the chemisorbed hydrogen that strongly interacts with hydrogen. The Ni/C-400 sample contains the highest amount of weakly chemisorbed Ni-Ni sites and the highest amount of moderately chemisorbed active Ni-O sites. Therefore, the catalytic performance can be significantly improved by enhancing the adsorption processes of hydrogen. H_2-TPR (temperature-programmed reduction) is a highly effective technique for studying the reduction behavior of supported oxide catalysts [50]. Hence, it was carried out to evaluate the reduction behavior of the Ni species in Ni/C-T samples (Fig. 6b). Impressively, obvious hydrogen consumption peaks can be seen for Ni/C-T samples. We inferred that the hydrogen consumption peak centered at 103 °C could belong to the chemisorbed hydrogen, whilst the peak in the range of 130–275 °C attributed to the highly dispersed surface NiO species in Ni/C-T samples (Fig. 6b). The hydrogen consumption calculated from the integrated areas of the corresponding H_2-TPR profiles is 3.89, 0.58, and 0.26 mmol·g^{-1} for Ni/C-400, Ni/C-500, and Ni/C-600 samples, respectively, which is highly related to the contents of surface NiO species (Fig. S34 and Table S8). The remarkable hydrogen consumption peak demonstrates the existence of abundant highly dispersed surface NiO sites in the
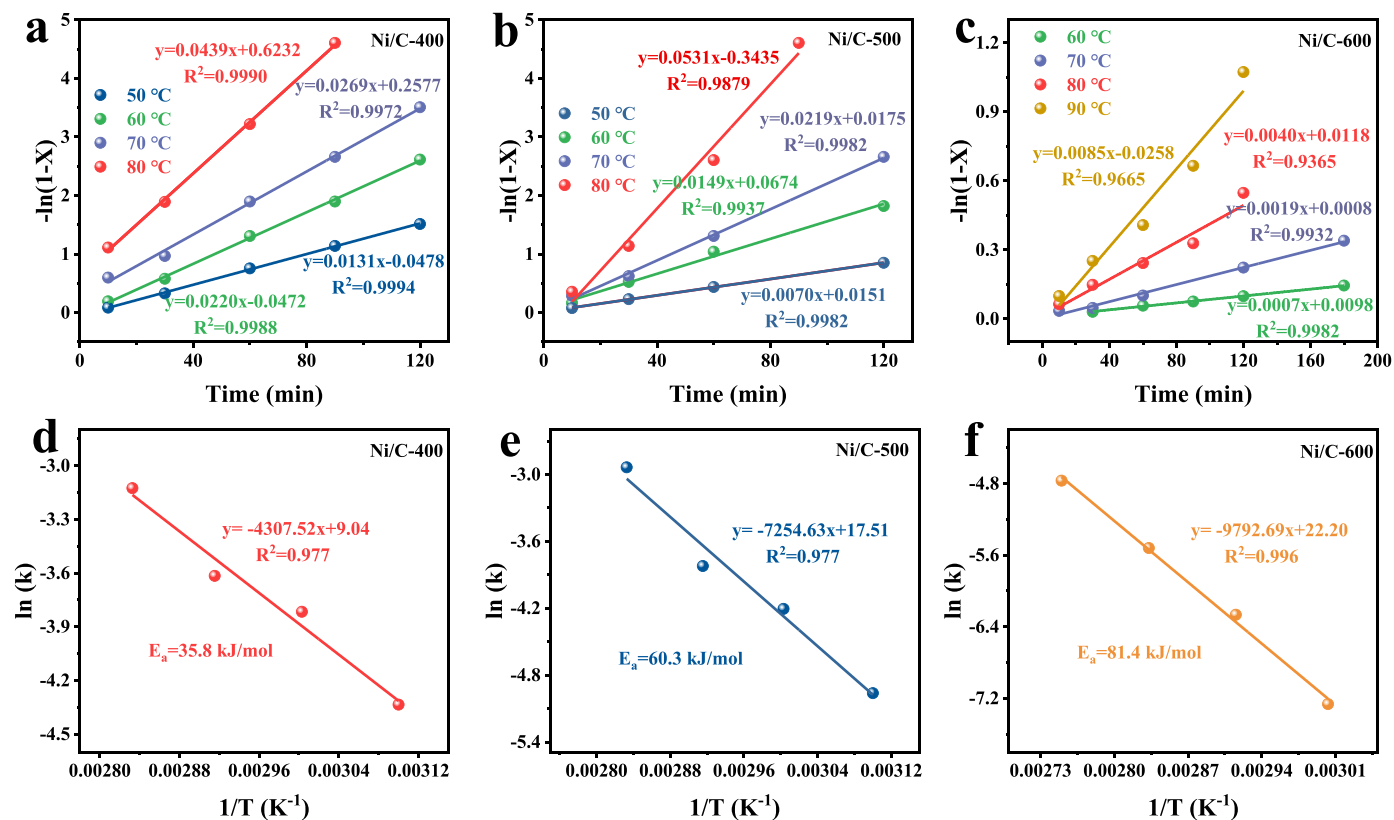
Fig. 5. First-order kinetic fit for the cascade reaction of FFR to THFA at different temperatures (333–353 K) for a) Ni/C-400, b) Ni/C-500 and c) Ni/C-600. The corresponding Arrhenius curve for d) Ni/C-400, e) Ni/C-500 and f) Ni/C-600. (Reaction conditions: 50 mL ethanol, 0.1 g catalyst, 1 MPa initial H_2 pressure).
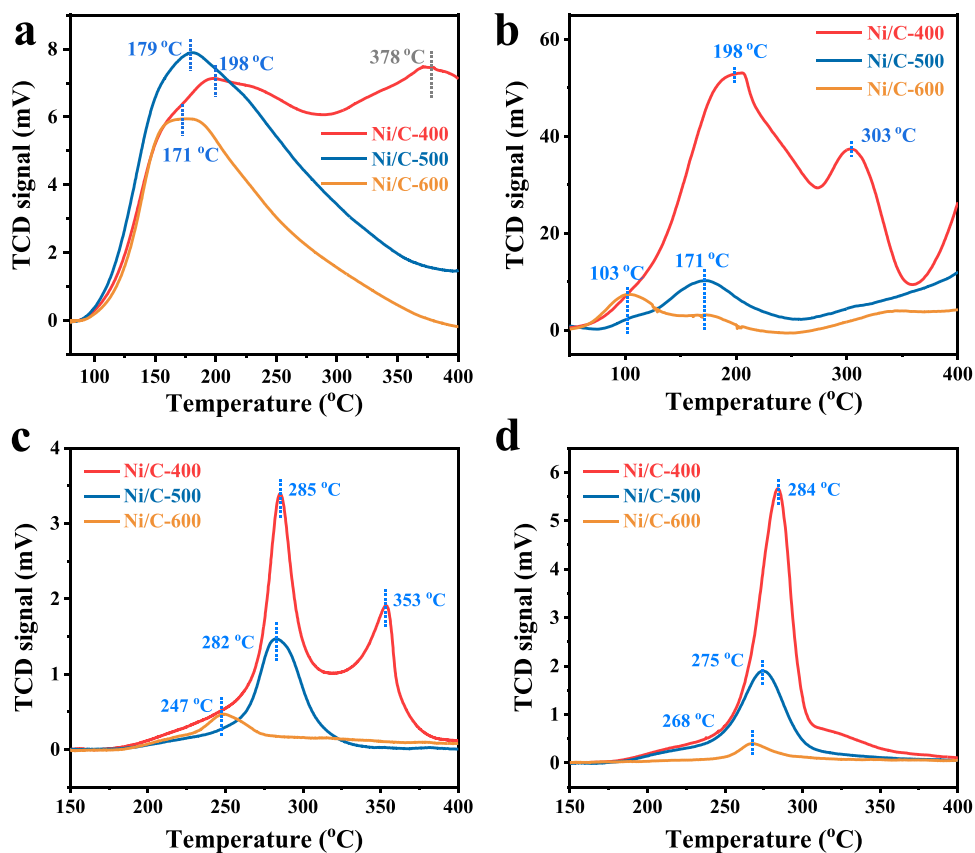

Fig. 6. a) H_2-TPD profiles, b) H_2-TPR curves, c) FFR-TPD profiles and d) FFA-TPD curves of Ni/C-T samples.

Ni/C-400 sample. Additionally, the peak around 303 °C for the Ni/C-400 is consistent with the peak position of bulk NiO species [9]. Since the bulk NiO species are encapsulated by the surface NiO species, it features a higher hydrogen reduction temperature.

The valence-state structure of Ni was further examined using ultra-violet photoelectron spectroscopy (UPS). All Ni/C-T samples have electron bands spanning the Fermi level (Fig. S35), indicating a metallic nature [51]. Besides, the peaks adjacent to the Fermi level belong to the 3d state of metallic Ni. From the d-band theory, the closer the Fermi energy level, the stronger the adsorption strength with the reactants [52]. Their positions, according to their binding energy, deviate from the Fermi level following the order: Ni/C-400 < Ni/C-500 < Ni/C-600. Therefore, the adsorption capacity with the reactants should follow the order: Ni/C-400 > Ni/C-500 > Ni/C-600.

A serious of purposely designed adsorption experiments were performed to identify the adsorption ability of Ni/C-T samples. For the first time, the temperature-programmed desorption of FFR (FFR-TPD) was conducted to explore FFR adsorption on Ni/C-T samples. As shown in Fig. 6c, a strong peak at 285 °C is observed in Ni/C-400, which could be assigned to the desorption of FFR molecules adsorbed on the surface of the catalytically active sites. Notably, another obvious peak located at 353 °C appeared, suggesting that there may be two different active sites (Ni particles and surface NiO species) in Ni/C-400 for FFR adsorption. The higher the desorption temperature, the stronger the chemical interaction between the FFR molecules and the catalysts. The desorption temperatures of Ni/C-400, Ni/C-500 and Ni/C-600 samples were progressively decreased from above 285–247 °C. Therefore, the Ni/C-400 sample has the highest ability to firmly grasp the FFR molecules to catalyze the hydrogenation reaction. In contrast, the lower desorption temperature of the Ni/C-600 sample implies the easy detachment of FFR molecules from samples, which is not conducive to the reaction. Besides, the integrated area of the desorption peak of the Ni/C-400 sample was significantly higher than that of other samples, representing the highest FFR adsorption capacity. To further confirm the high FFR adsorption capacity of Ni/C-400 sample, the TG test (mixing Ni/C-T with pure FFR) was conducted to study FFR adsorption on Ni/C-T (Fig. S36). The remarkable weight loss below 150 °C corresponds to physically adsorbed FFR molecules. In addition, the slight weight loss higher than 250 °C can be attributed to the chemisorbed FFR molecules at the catalytically active sites.

As an essential intermediate in FFR hydrogenation to THFA, the adsorption ability of FFA with active sites was also monitored, which was explored by the temperature-programmed desorption of FFA (FFA-TPD). Similar to FFR-TPD results, the peaks located below 300 °C could be attributed to the desorption of FFA molecules which have chemisorption capacity with the active sites (Fig. 6d). The desorption temperatures of Ni/C-400, Ni/C-500 and Ni/C-600 samples correspond to 284 °C, 275 °C and 268 °C, respectively, demonstrating that the FFA molecules are in close contact with Ni/C-400 for expediting the subsequent THFA generation process. Moreover, the highest FFA adsorption capacity of the Ni/C-400 sample can be inferred from the integrated area of the FFA desorption peak. Besides, TG test (FFA/Ni/C-T) also confirmed that the Ni/C-400 sample possessed the most robust chemisorption capacity and the highest FFA adsorption capacity (Fig. S37). From the above results, we speculated that the strong adsorption interaction between the FFA molecule and the catalysts is associated with the existence of abundant highly dispersed surface NiO species in the Ni/C-400 sample.

3.4. Theoretical study of surface NiO species for total hydrogenation of FFR

As the abovementioned adsorption tests confirmed, the outstanding catalytic performance of the Ni/C-400 catalyst could be closely related to the strong adsorption capacity between the active sites and reactants. To figure out the original catalytically active species, we attempted to correlate the catalytic performance of FFR hydrogenation with the Ni species in the catalyst. Surprisingly, compared to Ni^0 species, the content of $Ni^{2+, surf}$ is positively correlated with the THFA yield, indicating that it plays a crucial role in the catalytic activity (Fig. S38-40).

Theoretical analysis was conducted to understand the relationship between surface NiO species and the reactant's adsorption. According to the XRD, XPS and XANES results, the Ni/C-400 sample with abundant highly dispersed surface NiO sites is simplified to a Ni metal layer with an attached NiO cluster (denoted as Ni/NiO) (Fig. S41). Notably, the above-mentioned Ni/NiO interface is a transition state obtained by incomplete pyrolysis of Ni-BDC and cannot be detected by XRD, which is quite different from what has been reported in the literature. As a comparison, a pure Ni metal layer was selected (Fig. S42). The calculated isosurface of the deformation charge density suggests that the positive charge is mainly located around Ni metal layer due to the introduction of NiO cluster (Fig. 7a). Based on the calculated Bader charge (Table S9), the Ni metal layer possesses an atomic charge with electropositive or electronegative upon the presence of NiO cluster. This charge analysis results clearly indicate that the existence of surface NiO species affects the charge distribution of the Ni metal layer, which can substantially influence the adsorption and activation processes of the reactants.

It is well-established that FFR and H_2 adsorption are the key descriptors of FFR hydrogenation in the liquid phase. The adsorption energy of FFR on Ni/NiO is − 1.56 eV, much lower than that on the pure Ni metal layer (−0.44 V) (Fig. 7b and Fig. S43). Therefore, Ni/NiO with an inhomogeneous charge greatly facilitates the adsorption of FFR molecules, which may be due to the fact that the electronegative O atoms in the aldehyde and furan ring are susceptible to attachment by the electropositive Ni atoms. The H_2 molecules possess higher adsorption energy on Ni/NiO surface (−0.56 eV) than on Ni metal layer (−0.09 eV), indicating that H_2 is easily adsorbed on Ni surfaces with abundant highly-dispersed surface NiO species (Fig. 7c and Fig. S44). Moreover, the relatively short H-Ni bond length in Ni/NiO (1.588 Å/1.589 Å) compared to the Ni metal layer (1.591 Å/1.591 Å) also confirms the robust adsorption capacity between the H_2 molecule and Ni/NiO surface (Fig. S45). Meantime, the adsorption energy between the dissociated H atoms with Ni/NiO and Ni was − 1.26 eV and − 0.84 eV, respectively (Fig. 7c and Fig. S46). The H-Ni bond lengths in Ni/NiO (1.683 Å/ 1.695 Å/1.714 Å and 1.697 Å/1.684 Å/1.712 Å) are also shorter than those in the pure Ni metal layer (1.696 Å/1.699 Å/1.713 Å and 1.703 Å/1.704 Å/1.707 Å), indicating that the dissociated H atoms are firmly adsorbed on Ni/NiO (Fig. S47). Therefore, Ni metal layer with abundant highly-dispersed surface NiO species dramatically facilitates the adsorption activation of H_2 and FFR molecules. However, the relatively weak correlation between the content of surface NiO species and THFA yield ($R^2 = 0.766$) (Fig. S40) prompted us to explore other factors affecting catalyst activity.

3.5. Investigation of crystal facet for total hydrogenation of FFR

Numerous studies have shown that the carbonization temperature has a crucial effect on the carbonization degree of the carbon matrix formed by the in-situ transformation of organic ligands, the metal particle size or the species, which can affect the catalytic activity [53,54]. However, the effect of annealing temperature on the exposed crystal surface of metal particles has not been reported in the literature to the best of our knowledge. Therefore, the HRTEM test was performed to investigate the crystallographic orientation of Ni particles in Ni/C-T samples. As shown in Fig. 8, the thickness of the carbon layer in Ni/C-T samples increases with increasing the annealing temperature. The carbon layer, obtained by the transformation of organic ligand, does not cover the Ni particles from the unambiguous crystal facet, but slowly reduces highly-dispersed surface NiO to metallic Ni, which has been discussed previously. Through observing and analyzing the lattice fringes of the HRTEM patterns, the exposed facets of metallic Ni in the
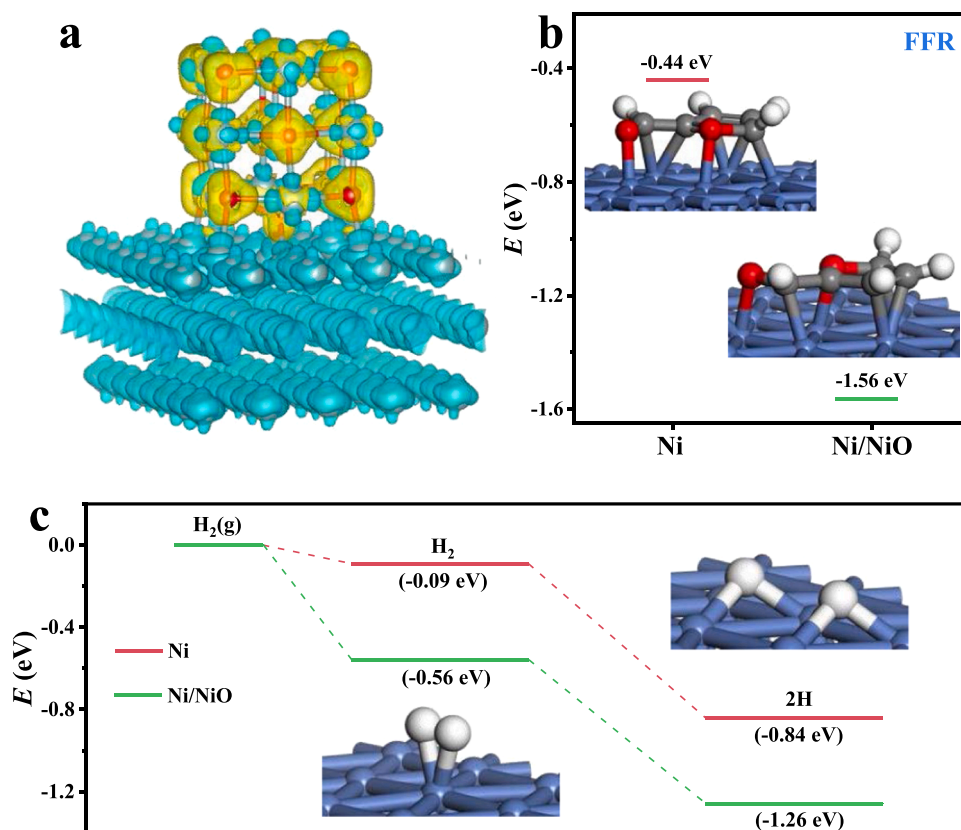
Fig. 7. a) Isosurface of the deformation charge density of Ni/NiO from the side view. Yellow and blue represent charge accumulation and loss, respectively. The isosurface is 0.01 a.u. b) The calculated adsorption energy of FFR molecule on Ni and Ni/NiO surfaces. c) The energy profiles of H_2 adsorption on Ni and Ni/NiO crystal surfaces. The Ni, O, C and H atoms are given in bluish violet, red, gray and white, respectively.
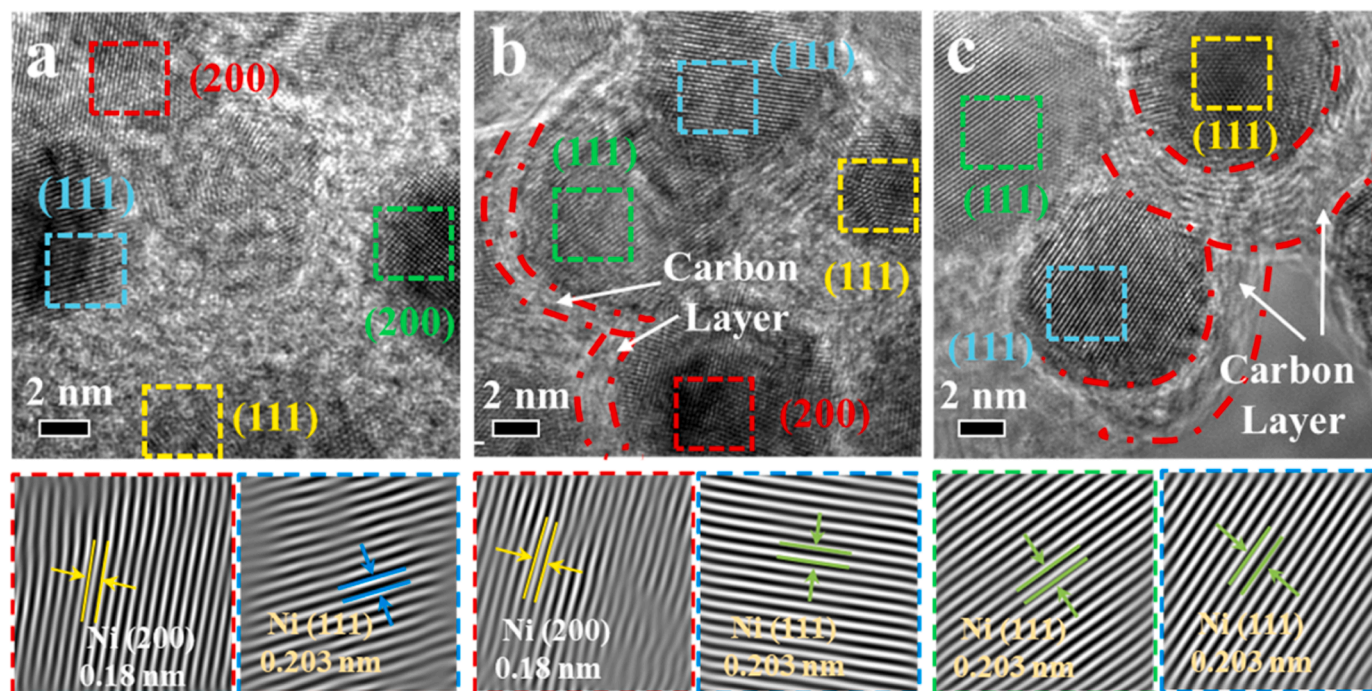

Fig. 8. HRTEM images of a) Ni/C-400, b) Ni/C-500, c) Ni/C-600 (The inverse fast Fourier transformation (IFFT) images taken from the selected areas indicated by a different color and the color of the figure edge corresponds to the color of the selected areas).

Ni/C-T samples were determined. From the enlarged images of Ni/C-400 (Below in Fig. 8a, which were selected from the areas denoted by the rectangles in Fig. 8a), the lattice spacings of 0.203 nm and 0.18 nm can be observed that are assigned to the (111) and (200) plane of metallic Ni, respectively (Fig. 7a and Fig. S48). Apparently, the ratio of exposed Ni (200) facets and Ni (111) facets was comparable in the Ni/C-400 sample, while less exposed Ni (200) facets were found in the Ni/C-500 sample (Fig. 8b-c and Fig. S49-50). Therefore, increasing the heat treatment temperature was detrimental to the exposure of the Ni (200) facets. In the case of the Ni/C-600 sample, only (111) planes of Ni^0 could be found. Although XRD results showed that Ni/C-600 displays a strong diffraction peak of Ni (200) facet, they cannot be exposed. Considering the relatively weak hydrogenation activity of Ni/C-600, it prompted us to thoroughly investigate the correlation between the exposed crystal facet and the catalytic performance. In addition, the texture coefficient (TC) of the (200) plane was calculated according to previous reports [55,56]. The TC (200) values for Ni/C-400, Ni/C-500 and Ni/C-600 were measured to be 1.04, 1.02 and 0.95, respectively, implying that the proportion of the (200) plane gradually decreases (Table S10). Therefore, the exposed facet can be easily tuned by adjusting the carbonization temperature, and the (200) crystal plane can easily be exposed at lower temperatures. Theoretically, metal atoms at different exposed facets have different coordination numbers, which are related to the adsorption energy of the reactant molecules. Therefore, it can be inferred that the (200) crystal plane (coordination number 8) might have a higher capacity to adsorb reactant molecules than that of the (111) crystal plane (coordination number 9), which is highly related to catalytic performance.

Density functional theory (DFT) calculations were carried out to uncover the adsorption behavior of substrates on different crystal facets. It has been reported that FFR adsorption on the Ni surface mainly adopts the parallel orientation [48,57]. According to HRTEM results, the Ni (200) and Ni (111) facet, which stands for the surface characteristic of Ni/C-T samples, were selected for subsequent calculations (Fig. S51). In the case of the Ni (111) facet (Fig. S52a), the C=O bond of the aldehyde group is bridge adsorbed on the top site of Ni atoms and the furan ring is parallel adsorbed on the surface of two 3-fold hollow sites, demonstrating the FFR molecules undergo active adsorption. As for Ni (200) facet (Fig. S52b), due to the change of facet, the furan ring adopts parallel to the surface of the 4-fold hollow sites. Theoretically, the geometric effect imposes an important influence on the catalytic performance of samples. The O1(O2) are chemically adsorbed on the terrace sites of the Ni (200) facet (coordination number: 8) with the Ni-O1(O2) bond length of 1.908 Å (2.043 Å), which is shorter than that of Ni (111) facet (coordination number: 9) with the Ni-O1(O2) bond length of 1.943 Å (2.089 Å) (Fig. S53-55 and Table S11). The above results indicated that there exists a stronger interaction between the FFR molecules and Ni (200) facet, promoting the adsorption and activation of both the C=O group and the furan ring, consistent with the consequence of FFR-TPD.

As reported, the d-band center can reflect the interaction of the adsorbate and active sites. The d-band center theory indicates that the electron density proximate to the Fermi level can impact the binding energy of the reaction intermediate [58]. The closer to the Fermi level, the stronger the adsorption interaction [59]. Based on the calculated PDOS, it is found that the electron density on the Ni (200) surface is higher than that on the Ni (111) surface near the Fermi level (Fig. S56). In addition, the d-band center of Ni (200) (-1.72 eV) displayed upshift
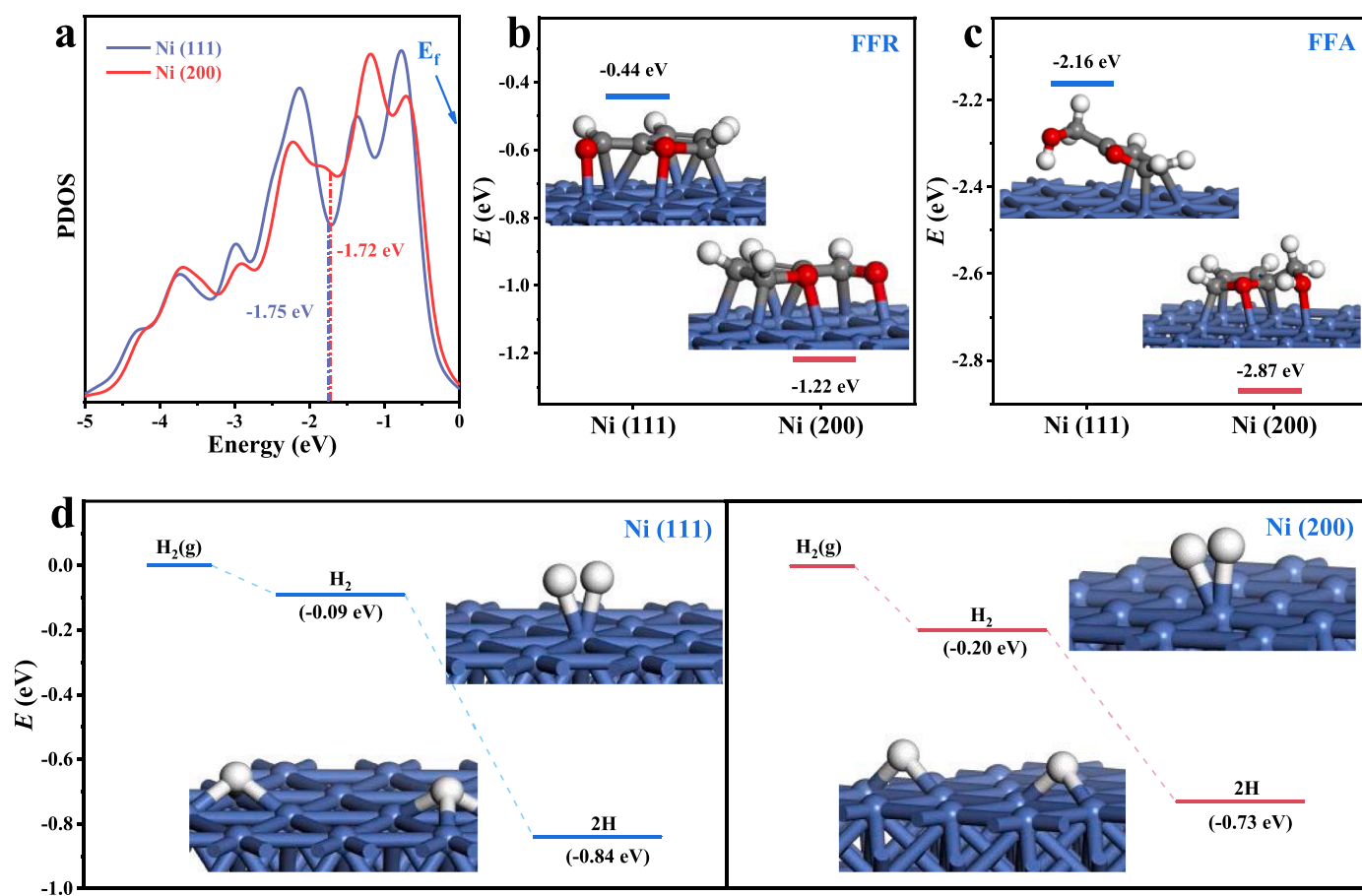

Fig. 9. a) Projected density of states (PDOS) plots of Ni (111) and Ni (200) (d-band center is highlighted in the PDOS curve). The calculated adsorption energy of b) FFR molecule and c) FFA molecule. d) The energy profiles of H_2 adsorption on Ni (111) and Ni (200) crystal surfaces. The Ni, O, C and H atoms are given in bluish violet, red, gray and white, respectively.

energy than that of the Ni (111) (−1.75 eV), suggesting a strong interaction between the Ni (200) surface and the adsorbate (Fig. 9a). The activation adsorption energies of FFR molecules on the Ni (200) and Ni (111) surfaces were calculated to be − 1.22 eV and − 0.44 eV, respectively (Fig. 9b). Therefore, the higher d-band center of Ni (200) surface leads to the FFR being adsorbed tightly to the active sites, thereby enhancing the hydrogenation activity [60]. Obviously, simple heat treatment can change the exposed facet of Ni particles, tune the coordination number of Ni atoms and modulate the d-band structure of the active sites, ultimately affecting the surface adsorption energy.

As mentioned above, FFA is the intermediate product of the total hydrogenation process, and the adsorption capacity determines the conversion path of FFR hydrogenation. When FFA is difficult to be detached from the catalyst surface, further hydrogenation of the furan ring can quickly occur to obtain THFA. Therefore, DFT calculations were performed to explore the adsorption configuration and adsorption energy of FFA on the Ni (111) and Ni (200) facets. The adsorption of FFA on the Ni (111) facet prefers to adopt a tilted adsorption mode with the furan ring as the bridging site, while FFA tends to exploit a flat orientation on Ni (200) surface (Fig. S57). Specifically, the tilted adsorption can weaken the interaction between the furan ring and metal sites, which restricts the furan ring from activating quickly and consequently converts FFA to THFA. As shown in Fig. 9c, the adsorption energy of FFA on Ni (111) and Ni (200) surface are − 2.06 eV and − 2.87 eV, respectively, which manifests that the adsorption of the FFA molecule is enhanced on the surface of Ni (200), leading to an easier activation of the furan ring to obtain THFA.

As H₂ plays a vital role in the hydrogenation process, the adsorption behavior of hydrogen on Ni (111) and Ni (200) surface was investigated. DFT calculations indicate that H₂ molecule is adsorbed on the Ni top sites, with the Ni-H bond length of 1.591 Å (1.591 Å) and 1.584 Å (1.577 Å) for the Ni (111) and Ni (200) surface, respectively, demonstrating that the H₂ molecule is tightly attached on Ni (200) surface (Fig. S58-60). The shorter bond length between Ni-H indicates that the active Ni site is capable of adsorbing FFR/FFA along with H₂ molecules simultaneously, ensuring an efficient and quick hydrogenation reaction. Furthermore, the adsorption energy of H₂ on Ni (111) and Ni (200) surface are calculated to be − 0.09 eV and − 0.2 eV, respectively (Fig. 9d), which indicates that H₂ is preferentially adsorbed on the Ni (200) surface and subsequently dissociated to H atoms participating in the hydrogenation process. Correspondingly, the adsorption behavior of activated H atoms after the dissociation of H₂ molecules was also studied. The activated H atoms on the Ni (111) surface are adsorbed on the surface of 3-fold hollow sites, while on the Ni (200) surface they are bridged to 2-fold Ni sites (Fig. S61). Moreover, the adsorption energy of activated H atoms on the Ni (111) and Ni (200) surfaces corresponded to − 0.84 eV and − 0.73 eV, respectively (Fig. 9d). The dissociation of H₂ molecules to activated H atoms on Ni (200) surface has a lower energy barrier, indicating that activated H atoms are easy to form on Ni (200) surface.

Ni (200) facet, possessed a lower coordination number of Ni atoms and higher d-band center, has an enhanced ability to adsorb FFR, FFA and H₂ molecules, as well as form activated H atoms, which can dramatically reduce the adsorption energy of the reactants and promotes the activity of the hydrogenation reaction. Therefore, the difference in exposed crystal facets in the samples is another crucial factor affecting the catalytic activity. The poorer hydrogenation performance of the Ni/C-600 sample is closely related to the absence of exposed Ni (200) facets. Meantime, the presence of abundant highly dispersed surface NiO species and exposed Ni (200) facets empower the Ni/C-400 sample with superior catalytic activity for FFR hydrogenation.

In situ FT-IR measurements were conducted to study FFR adsorption on the surface of the Ni/C-400 sample. As shown in Fig. 10a, three peaks positioned at 1719 cm⁻¹, 1584 cm⁻¹, and 1474 cm⁻¹ assigned to ν(C=O), aromatic ring breath and ν(C=C), respectively [17]. After the introduction of FFR in the Ni/C-400 sample, an obvious red-shift from 1719 cm⁻¹ to 1663 cm⁻¹ of ν(C=O) was observed, which confirmed that the Ni/C-400 sample greatly activated the C=O group. Besides, the disappearance of the peaks belongs to aromatic ring breath and ν(C=C) proved the strong chemical adsorption between the furan ring and the Ni/C-400. The above result verified that both C=O and furan ring strongly chemisorbed on Ni sites, which is consistent with the results of parallel adsorption of FFR molecules on the catalyst surface in DFT calculations. Subsequently, the changes in reactants and products during FFR hydrogenation from room temperature to 80 °C were monitored by introducing H₂ into the reaction cell using in situ FT-IR spectroscopy. Obviously, the band at 1663 cm⁻¹ (C=O) delines gradually with the rising reaction temperature, while a new band (1122 cm⁻¹) belonging to the C-O group is formed and gradually strengthens, confirming the hydrogenation process of the FFR (Fig. 10b and Fig. S62).

3.6. Optimized experiments toward total hydrogenation of FFR

According to the above-mentioned results, it is known that the Ni/C-400 catalysts can effectively catalyze FFR to THFA (Fig. 11a). Then, the catalytic activity of Ni/C-400 catalysts was further evaluated to obtain an optimal reaction condition for FFR hydrogenation. Firstly, the effect of reaction temperature was explored under 1 MPa initial H₂ pressure
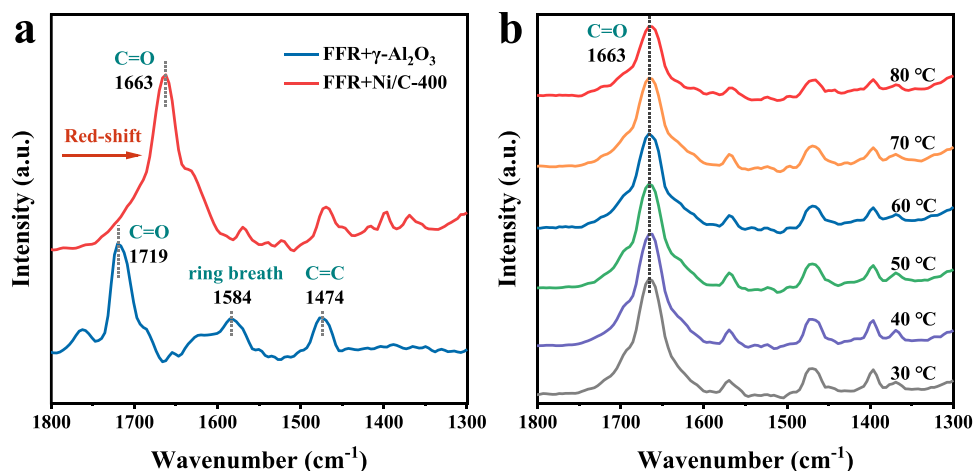

Fig. 10. a) In situ FT-IR spectra of the gas phase of FFR adsorbed on γ-Al₂O₃ and Ni/C-400, recorded after flowing FFR for 30 min at room temperature and subsequent helium flushing for 30 min b) In situ FT-IR spectra for hydrogenation process of FFR on Ni/C-400 via flowing H₂ as a reaction gas, recorded at 30 °C, 40 °C, 50 °C, 60 °C, 70 °C and 80 °C, respectively.
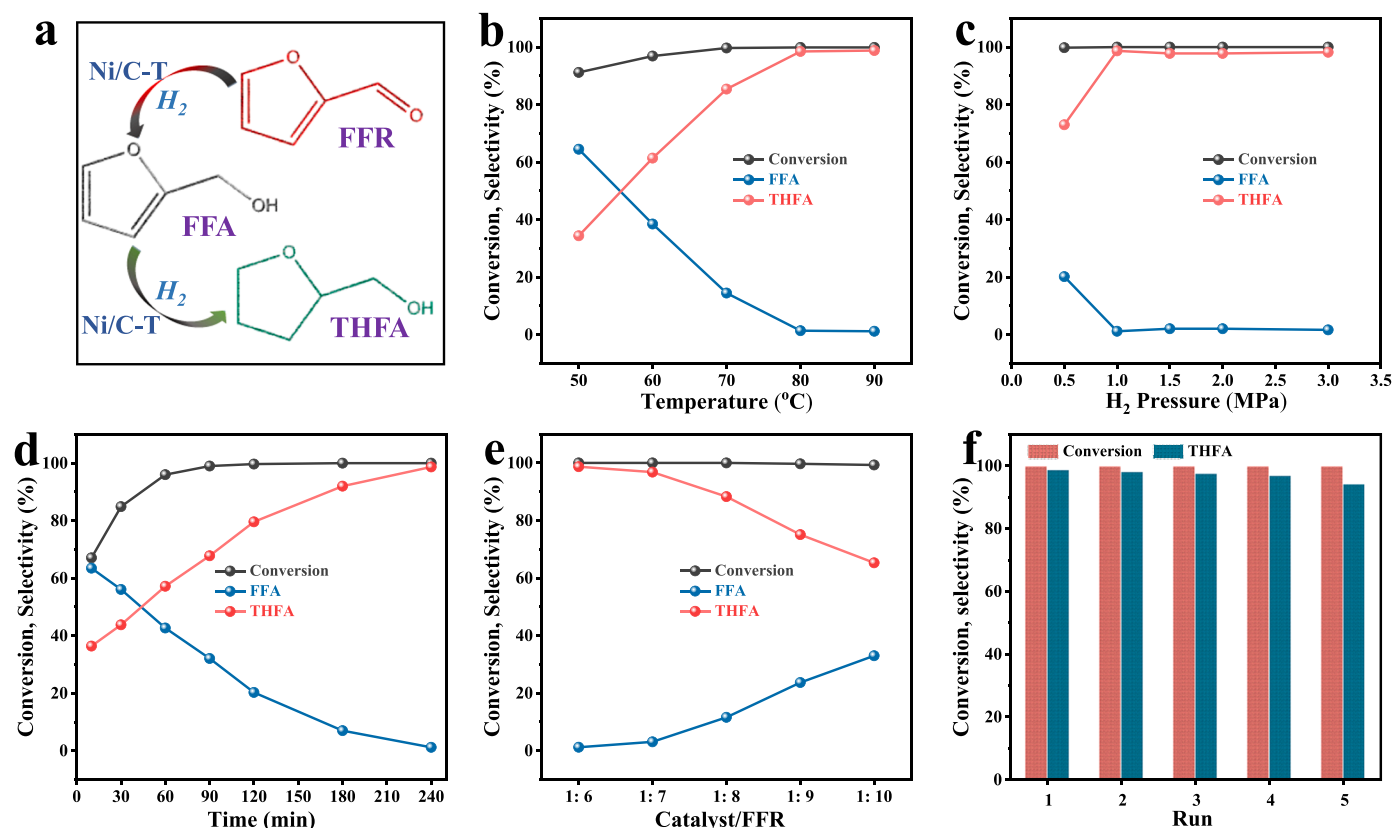
Fig. 11. a) Schematic illustration for hydrogenation of FFR into THFA; b) Effect of reaction temperatures (1 MPa initial H_2 pressure, 4 h, 0.6 g FFR); c) Effect of H_2 pressure (80 °C, 4 h, 0.6 g FFR); d) Effect of reaction time (80 °C, 1 MPa initial H_2 pressure, 0.6 g FFR); e) Effect of FFR concentration (1 MPa initial H_2 pressure, 80 °C, 4 h, 0.6 g FFR); f) the reusability of the Ni/C-400 catalyst (1 MPa H_2, 80 °C, 4 h, 0.6 g FFR). Other reaction conditions: 50 mL ethanol, 0.1 g Ni/C-400 catalyst.

for 4 h (Fig. 11b). The FFR conversion was found to increase from 91.2 % to 99.9 %, while the selectivity of THFA increased from 34.4 % to 98.5 % as the reaction temperature increased from 50 °C to 80 °C and leveled off with further increased reaction temperature. Therefore, the hydrogenation on C=O is easier than that of C=C under relatively low temperatures, whereas high temperatures can accelerate the occurrence of hydrogenation in both C=O and furan rings. The effect of reaction H_2 pressure was then evaluated under 80 °C for 4 h. As revealed in Fig. 11c, when the initial H_2 pressure was increased from 0.5 to 1 MPa at 80 °C, the FFR conversion remained consistently at a high value (99.9 %), but the THFA selectivity was significantly improved from 73 % to 98.5 %. The lower THFA selectivity of the reaction at 0.5 MPa H_2 pressure is due to the depletion of the hydrogen in the reactor (Fig. S63). The H_2 pressure was maintained at 0.5 MPa by adding hydrogen in the reaction process, and 94 % THFA yield can be achieved under 80 °C for 4 h (Table 1, Entry 8), which indicated that the Ni/C-400 catalyst had a high capacity to dissolve hydrogen even at lower H_2 pressure. The catalytic activity displayed a neglectable increase with increasing the H_2 pressure. Thus, 1 MPa was selected as the optimal H_2 pressure. Fig. 11d shows the effect of reaction time for Ni/C-400 under 80 °C and 1 MPa initial H_2 pressure. The FFR conversion increased with increasing the reaction time, and an almost complete conversion could be obtained after 90 min. In contrast, the THFA selectivity increased to 80 % in 2 h, and a further increase in the reaction time resulted in a conversion from 80 % to 98.5 % in the next 2 h, which ranks it the best among the reported non-noble catalysts (Table S12). Although there have been several reports on the conversion of FFR to THFA, all exhibiting good performance, most of which fail in combining low reaction temperature with low reaction hydrogen pressure. For example, although the catalyst prepared by Su et al. showed high THFA yields, its reaction temperature was more demanding (Table S12, Entry 3) [61]. To the best of our

knowledge, high-efficient non-noble catalysts like Ni/C-400 prepared in our work, combining low reaction temperature as well as reaction hydrogen pressure for total hydrogenation of FFR, have not been reported. In addition, the catalyst performance in FFR substrate concentration was studied (Fig. 11e). The results showed that the FFR conversions all exceeded 99 % at the selected FFR concentrations. The selectivity of THFA (96.8 %) decreased slightly when the mass ratio of FFR/Ni/C-400 was increased to 7. Nevertheless, an increase in the mass ratio of FFR/Ni/C-400 from 7 to 10 resulted in a linearly decreased THFA selectivity to 65 %. The above results indicated that the higher the FFR dosage, the lower the THFA selectivity, which was due to the massive blockage at catalytic active sites [4]. Many researchers have demonstrated that the solvent plays a crucial role in determining product distribution in the hydrogenation of FFR, for example, one recent study has shown that FFR is predominantly converted to CPO in water [62]. Therefore, the effect of solvent on the selectivity of the products was carried out. The results indicated that methanol, ethanol and n-butanol yielded THFA with high selectivity, whereas n-propanol, isopropanol and water failed to generate THFA (Table S13).

Reusability is one of the most critical indicators for evaluating the performance of catalysts. Therefore, the Ni/C-400 catalyst was used five times under the same optimal reaction conditions (Fig. 11f). After several successive reactions, only a negligible loss of reaction activity could be seen. The main deactivation reason could be that the residual products on the surface of the catalyst were not completely cleaned, leading to the difficulty of effectively utilizing partial catalytic sites. The well-maintained catalytic activity after five consecutive cycles demonstrated the high stability and reusability of Ni/C-400. XRD results and TEM images displayed non-obvious changes in the structure and no aggregation of metal particles was observed in the used catalysts (Fig. S64-65). Additionally, the specific surface area, total pore volume

and the position of Ni species of the Ni/C-400 sample were almost the same before and after the reaction, also verifying the robustness of the Ni/C-400 catalyst (Fig. S66-67). The leaching test showed that the elemental Ni content in the solution after the reaction was almost undetectable, which further confirmed the excellent thermal stability of the Ni/C-400 sample (Table S14).

3.7. Investigation of substrates scope

The aforementioned studies suggested that the as-synthesized Ni/C-400 catalyst afforded promising activity in the ethanol-phase hydrogenation of FFR. Therefore, we conjecture that it also has exceptional catalytic activity for other unsaturated aldehydes and ketones. To validate our hypothesis, a series of purposely designed experiments were performed, and the results are summarized in Table 2. It can be seen that Ni/C-400 exhibited excellent catalytic activities for all listed compounds. The Ni/C-400 catalyst gave 92.4 % 2-methylfuran conversion and 92.5 % 2-methyltetrahydrofuran selectivity at 80 °C for 4 h (Table 2, Entry 2). Besides, it was effective towards nitro compounds, complete conversion of nitrobenzene and 93.9 % selectivity of aniline were obtained (Table 2, Entry 3). Amazingly, Ni/C-400 is highly efficient in the deep reduction of benzaldehyde to toluene, giving a 99.5 % yield of toluene within 3 h (Table 2, Entry 4). Also, it has significant hydrogenation activity against straight-chain aldehydes. The yield of n-butanol and n-amyl alcohol reached 98 % and 96.6 % within 2 h and 4 h, respectively, indicating that the reaction rate was slowed down by the longer carbon chain length (Table 2, Entry 5–6). Impressively, cyclic ketones such as cyclohexanone and cycloheptanone can be 100 % and 92.2 % converted to corresponding alcohols within 4 h and 10 h, respectively (Table 2, Entry 7–8). The above results indicated that the as-synthesized Ni/C-400 catalysts could be widely applied to a wide range of catalytic applications.

4. Conclusion

In summary, Ni/C-T catalysts with adjustable surface NiO species and variable exposed Ni facets were prepared by employing 3D flower-like Ni-BDC as the precursor. 2D ultrathin nanosheets were demonstrated to be effective in confining the size of Ni nanoparticles and enhancing the exposure of catalytic active sites. The Ni/C-400 sample with a low E_a value of 35.8 kJ·mol^{-1} displayed remarkable catalytic performance for the hydrogenation reaction of various biomass-derived platform molecules; notably, an extremely high yield of 98.5 % was achieved for one-step total hydrogenation of FFR under moderate conditions. Importantly, we theoretically and experimentally verified that the distinguished catalytic performance is attributed to the difference in exposed facets and the distributions of surface NiO species. FFA/FFR-TPD tests were employed for the first time to study the adsorption interaction between reactants and catalytic active sites, in accordance with the theoretical results. Ni particles with surface NiO species and Ni (200) facets have a stronger ability to adsorb reactants, which is an important reason to facilitate the efficient conversion of FFR to THFA. Meanwhile, Ni (200) facets can significantly facilitate the dissociation of H_2 molecules. The highly exposed Ni (200) facets with abundant surface NiO species synergistically empower the Ni/C-400 sample with remarkable catalytic activity. The findings of this work substantiated the enhancement of the adsorption capacity between reactants and active catalytic sites via tailoring the surface NiO species and exposed metal facet, which can be extended to design more efficient catalysts for biomass-upgrading reactions.
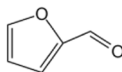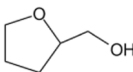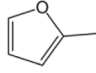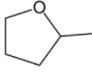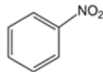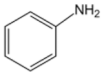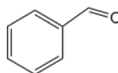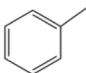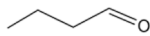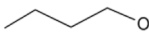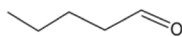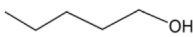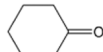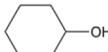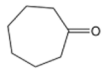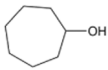
CRediT authorship contribution statement

Qiuju Fu: Investigation, Writing – original draft. **Liting Yan:** Methodology, Supervision, Data curation, Funding acquisition. **Dandan Liu:** Investigation. **Shuo Zhang:** Software. **Huimin Jiang:** Resources. **Wenpeng Xie:** Formal analysis. **Lingzhi Yang:** Resources. **Yujia Wang:** Resources. **Haiyan Wang:** Supervision. **Xuebo Zhao:** Conceptualization, Supervision, Funding acquisition, Writing – review & editing.

Declaration of Competing Interest

The authors declare that they have no known competing financial interests or personal relationships that could have appeared to influence

Table 2
The catalytic performance of Ni/C-400 catalyst for different substrates.

Entry	Substrates	Products	Time (h)	Conversion (%)	Selectivity (%)
1			4	100	98.5
2			4	92.4	92.5
3			4	100	93.9
4			3	100	99.5
5			2	98	99.1
6			4	96.6	99.9
7			4	100	99.9
8			10	92.2	99.9

Reaction conditions: 0.6 g substrates; 0.1 g catalysts; 50 mL of ethanol; 80 °C; 1 MPa initial H_2 pressure.

the work reported in this paper.

Data availability

Data will be made available on request.

Acknowledgements

Appendix A. Supporting information

Supplementary data associated with this article can be found in the online version at doi:10.1016/j.apcatb.2023.123501.

References

[1] X. Li, P. Jia, T. Wang, Furfural: a promising platform compound for sustainable production of C_4 and C_5 chemicals, ACS Catal. 6 (2016) 7621–7640, https://doi.org/10.1021/acscatal.6b01838.

[2] J.J. Bozell, G.R. Petersen, Technology development for the production of biobased products from biorefinery carbohydrates–the US Department of Energy's "Top 10" revisited, Green Chem. 12 (2010) 539–554, https://doi.org/10.1039/b922014c.

[3] Q. Fu, H. Jiang, Y. Wang, H. Wang, X. Zhao, Recent advances in metal-organic framework based heterogeneous catalysts for furfural hydrogenation reactions, Mater. Chem. Front. 7 (2023) 628–642, https://doi.org/10.1039/d2qm01181f.

[4] Q. Fu, D. Liu, W. Niu, S. Zhang, R. Chen, Y. Wang, P. Zhao, H. Jiang, Y. Zhao, L. Yang, L. Yan, H. Wang, X. Zhao, Defect-engineered MOF-808 with highly exposed Zr sites as highly efficient catalysts for catalytic transfer hydrogenation of furfural, Fuel 327 (2022), 125085, https://doi.org/10.1016/j.fuel.2022.125085.

[5] W. Fang, S. Liu, A.K. Steffensen, L. Schill, G. Kastlunger, A. Riisager, On the role of Cu^+ and CuNi alloy phases in mesoporous CuNi catalyst for furfural hydrogenation, ACS Catal. 13 (2023) 8437–8444, https://doi.org/10.1021/acscatal.3c01767.

[6] Y. Peng, Z. Xu, L. Yu, X. Li, W. Yang, Trimetallic Cu-Ni-Re/Hβ catalyst for the direct conversion of furfural to 2-Methyltetrahydrofuran, Chem. Eng. J. 454 (2023), https://doi.org/10.1016/j.cej.2022.139746.

[7] R. Bavisotto, S.P. Roy, N. Hopper, W.T. Tysoe, Understanding hydrogen pressure control of furfural hydrogenation selectivity on a Pd(111) model catalyst, J. Catal. 421 (2023) 55–64, https://doi.org/10.1016/j.jcat.2023.03.010.

[8] L. Ruan, A. Pei, J. Liao, L. Zeng, G. Guo, K. Yang, Q. Zhou, N. Zhao, L. Zhu, B. H. Chen, Nitrogen-doped carbon nanotubes-supported PdNiCo nanoparticles as a highly efficient catalyst for selective hydrogenation of furfural, Fuel 284 (2021), 119015, https://doi.org/10.1016/j.fuel.2020.119015.

[9] S. Li, Y. Wang, L. Gao, Y. Wu, X. Yang, P. Sheng, G. Xiao, Short channeled Ni-Co/SBA-15 catalysts for highly selective hydrogenation of biomass-derived furfural to tetrahydrofurfuryl alcohol, Microporous Mesoporous Mater. 262 (2018) 154–165, https://doi.org/10.1016/j.micromeso.2017.11.027.

[10] Y. Cao, H. Zhang, K. Liu, Q. Zhang, K. Chen, Biowaste-derived bimetallic Ru-MoO$_x$ catalyst for the direct hydrogenation of furfural to tetrahydrofurfuryl alcohol, ACS Sustain. Chem. Eng. 7 (2019) 12858–12866, https://doi.org/10.1021/acssuschemeng.9b01765.

[11] S. Campisi, C.E. ChanThaw, L.E. Chinchilla, A. Chutia, G.A. Botton, K.M. H. Mohammed, N. Dimitratos, P.P. Wells, A. Villa, Dual-site-mediated hydrogenation catalysis on Pd/NiO: Selective biomass transformation and maintenance of catalytic activity at low Pd loading, ACS Catal. 10 (2020) 5483–5492, https://doi.org/10.1021/acscatal.0c00414.

[12] D. Hu, H. Xu, Z. Yi, Z. Chen, C. Ye, Z. Wu, H.F. Garces, K. Yan, Green CO_2-assisted synthesis of mono- and bimetallic Pd/Pt nanoparticles on porous carbon fabricated from sorghum for highly selective hydrogenation of furfural, ACS Sustain. Chem. Eng. 7 (2019) 15339–15345, https://doi.org/10.1021/acssuschemeng.9b02665.

[13] Babasaheb M. Matsagar, Chang-Yen Hsu, Season S. Chen, Tansir Ahamad, Saad M. Alshehri, D.C.W. Tsang, K.C.W. Wu, Selective hydrogenation of furfural to tetrahydrofurfuryl alcohol over a Rh-loaded carbon catalyst in aqueous solution under mild conditions, Sustain. Energy Fuels 4 (2020) 293–301, https://doi.org/10.1039/C9SE00681H.

[14] Y. Long, S. Song, J. Li, L. Wu, Q. Wang, Y. Liu, R. Jin, H. Zhang, Pt/CeO$_2$@MOF core@shell nanoreactor for selective hydrogenation of furfural via the channel screening effect, ACS Catal. (2018) 8506–8512, https://doi.org/10.1021/acscatal.8b01851.

[15] J. Xu, Q. Cui, T. Xue, Y. Guan, P. Wu, Total hydrogenation of furfural under mild conditions over a durable Ni/TiO$_2$-SiO$_2$ catalyst with amorphous TiO$_2$ species, ACS Omega 5 (2020) 30257–30266, https://doi.org/10.1021/acsomega.0c04736.

[16] J. Parikh, S. Srivastava, G.C. Jadeja, Selective hydrogenation of furfural to tetrahydrofurfuryl alcohol using supported nickel-cobalt catalysts, Ind. Eng. Chem. Res. 58 (2019) 16138–16152, https://doi.org/10.1021/acs.iecr.9b01443.

[17] X. Meng, Y. Yang, L. Chen, M. Xu, X. Zhang, M. Wei, A control over hydrogenation selectivity of furfural via tuning exposed facet of Ni catalysts, ACS Catal. 9 (2019) 4226–4235, https://doi.org/10.1021/acscatal.9b00238.

[18] K.L. MacIntosh, S.K. Beaumont, Nickel-catalysed vapour-phase hydrogenation of furfural, Insights into reactivity and deactivation, Top. Catal. 63 (2020) 1446–1462, https://doi.org/10.1007/s11244-020-01341-9.

[19] R. Insyani, A.F. Barus, R. Gunawan, J. Park, G.T. Jaya, H.S. Cahyadi, M.G. Sibi, S. K. Kwak, D. Verma, J. Kim, RuO$_2$-Ru/Hβ zeolite catalyst for high-yield direct conversion of xylose to tetrahydrofurfuryl alcohol, Appl. Catal. B 291 (2021), https://doi.org/10.1016/j.apcatb.2021.120120.

[20] X. Zhao, B. Xiao, A.J. Fletcher, K.M. Thomas, D. Bradshaw, M.J. Rosseinsky, Hysteretic adsorption and desorption of hydrogen by nanoporous metal-organic frameworks, Science 306 (2004) 1012–1015, https://doi.org/10.1126/science.1101982.

[21] L. Yang, L. Yan, W. Niu, Y. Feng, Q. Fu, S. Zhang, Y. Zhang, L. Li, X. Gu, P. Dai, D. Liu, Q. Zheng, X. Zhao, Adsorption in reversed order of C_2 hydrocarbons on an ultramicroporous fluorinated metal-organic framework, Angew. Chem. Int. Ed. 61 (2022), e202204046, https://doi.org/10.1002/anie.202204046.

[22] L. Yan, Y. Xu, P. Chen, S. Zhang, H. Jiang, L. Yang, Y. Wang, L. Zhang, J. Shen, X. Zhao, L. Wang, A freestanding 3D heterostructure film stitched by MOF-derived carbon nanotube microsphere superstructure and reduced graphene oxide sheets: a superior multifunctional electrode for overall water splitting and Zn-Air batteries, Adv. Mater. 32 (2020), 2003313, https://doi.org/10.1002/adma.202003313.

[23] H. Jiang, S. Zhang, L. Yan, Y. Xing, Z. Zhang, Q. Zheng, J. Shen, X. Zhao, L. Wang, Stress-dispersed superstructure of Sn$_3$(PO$_4$)$_2$@PC derived from programmable assembly of metal-organic framework as long-life potassium/sodium-ion batteries anodes, Adv. Sci. 10 (2023), e2206587, https://doi.org/10.1002/advs.202206587.

[24] Y. Lv, M. Han, W. Gong, D. Wang, C. Chen, G. Wang, H. Zhang, H. Zhao, Fe-Co alloyed nanoparticles catalysed efficient hydrogenation of cinnamaldehyde to cinnamyl alcohol in water, Angew. Chem. Int. Ed. 59 (2020) 23521–23526, https://doi.org/10.1002/anie.202009913.

[25] Y. Fan, S. Li, Y. Wang, C. Zhuang, X. Liu, G. Zhu, X. Zou, Tuning the synthesis of polymetallic-doped ZIF derived materials for efficient hydrogenation of furfural to furfuryl alcohol, Nanoscale 12 (2020) 18296–18304, https://doi.org/10.1039/d0nr04098c.

[26] F. Tang, L. Wang, M. Dessie Walle, A. Mustapha, Y. Liu, An alloy chemistry strategy to tailoring the d-band center of Ni by Cu for efficient and selective catalytic hydrogenation of furfural, J. Catal. 383 (2020) 172–180, https://doi.org/10.1016/j.jcat.2020.01.019.

[27] Y. Tian, A. Huang, Z. Wang, M. Wang, Q. Wu, Y. Shen, Q. Zhu, Y. Fu, M. Wen, Two-dimensional hetero-nanostructured electrocatalyst of Ni/NiFe-layered double oxide for highly efficient hydrogen evolution reaction in alkaline medium, Chem. Eng. J. 426 (2021) 131827, https://doi.org/10.1016/j.cej.2021.131827.

[28] K. Ge, S. Sun, Y. Zhao, K. Yang, S. Wang, Z. Zhang, J. Cao, Y. Yang, Y. Zhang, M. Pan, L. Zhu, Facile synthesis of two-dimensional Fe/Co metal-organic framework for efficient oxygen evolution electrocatalysis, Angew. Chem. Int. Ed. 133 (2021) 12204–12209, https://doi.org/10.1002/anie.202102632.

[29] H. Yu, Y. Jing, C.-F. Du, J. Wang, Tuning the reversible chemisorption of hydroxyl ions to promote the electrocatalysis on ultrathin metal-organic framework nanosheets, J. Energy Chem. 65 (2022) 71–77, https://doi.org/10.1016/j.jechem.2021.05.029.

[30] L. Cao, P. Dai, J. Tang, D. Li, R. Chen, D. Liu, X. Gu, L. Li, Y. Bando, Y.S. Ok, X. Zhao, Y. Yamauchi, Spherical superstructure of boron nitride nanosheets derived from boron-containing metal-organic frameworks, J. Am. Chem. Soc. 142 (2020) 8755–8762, https://doi.org/10.1021/jacs.0c01023.

[31] J. Zhou, Y. Dou, T. He, A. Zhou, X.J. Kong, X.Q. Wu, T. Liu, J.R. Li, Revealing the effect of anion-tuning in bimetallic chalcogenides on electrocatalytic overall water splitting, Nano Res. (2021) 1–8, https://doi.org/10.1007/s12274-021-3370-7.

[32] G. Kresse, J. Furthmuller, Efficient iterative schemes for ab initio total-energy calculations using a plane-wave basis set, Phys. Rev. B Condens. Matter Mater. 54 (1996) 11169–11186, https://doi.org/10.1103/physrevb.54.11169.

[33] G. Kresse, J. Furthmiiller, Efficiency of ab-initio total energy calculations for metals and semiconductors using a plane-wave basis set, Comput. Mater. Sci. 6 (1996) 15–50, https://doi.org/10.1103/physrevb.54.11169.

[34] C. Qiang, M. Liu, L. Zhang, Z. Chen, Z. Fang, In situ growth of Ni-based metal-organic framework nanosheets on carbon nanotube films for efficient oxygen evolution reaction, Inorg. Chem. 60 (2021) 3439–3446, https://doi.org/10.1021/acs.inorgchem.1c00026.

[35] B. Wang, M. Zhao, L. Li, Y. Huang, X. Zhang, C. Guo, Z. Zhang, H. Cheng, W. Liu, J. Shang, J. Jin, X. Sun, J. Liu, H. Zhang, Ultrathin metal-organic framework nanoribbons, Natl. Sci. Rev. 7 (2019) 46–52, https://doi.org/10.1093/nsr/nwz118/5549056.

[36] Sharifeh Rezaeea, S. Shahrokhian, Facile synthesis of petal-like NiCo/NiO-CoO/nanoporous carbon composite based on mixed-metallic MOFs and their application for electrocatalytic oxidation of methanol, Appl. Catal. B 244 (2019) 802–813, https://doi.org/10.1016/j.apcatb.2018.12.013.

[37] Y. Zheng, R. Zhang, L. Zhang, Q. Gu, Z.A. Qiao, A resol-assisted cationic coordinative Co-assembly approach to mesoporous ABO$_3$ perovskite oxides with rich oxygen vacancy for enhanced hydrogenation of furfural to furfuryl alcohol, Angew. Chem. Int. Ed. (2020), https://doi.org/10.1002/anie.202012416.

[38] S. Zhang, P. Dai, H. Liu, L. Yan, H. Song, D. Liu, X. Zhao, Metal-organic framework derived porous flakes of cobalt chalcogenides (CoX, X = O, S, Se and Te) rooted in carbon fibers as flexible electrode materials for pseudocapacitive energy storage,

Electrochim. Acta 369 (2021), 137681, https://doi.org/10.1016/j.electacta.2020.137681.

[39] J. Li, W. Xia, J. Tang, Y. Gao, C. Jiang, Y. Jia, T. Chen, Z. Hou, R. Qi, D. Jiang, T. Asahi, X. Xu, T. Wang, J. He, Y. Yamauchi, Metal-organic framework-derived graphene mesh: a robust scaffold for highly exposed Fe-N$_4$ active sites toward an excellent oxygen reduction catalyst in acid media, J. Am. Chem. Soc. 144 (2022) 9280–9291, https://doi.org/10.1021/jacs.2c00719.

[40] L. Soriano, I. Preda, A. Gutiérrez, S. Palacín, M. Abbate, A. Vollmer, Surface effects in the Ni 2p x-ray photoemission spectra of NiO, Phys. Rev. B 75 (2007), 233417, https://doi.org/10.1103/PhysRevB.75.233417.

[41] M.A. Peck, M.A. Langell, Comparison of nanoscaled and bulk NiO structural and environmental characteristics by XRD, XAFS, and XPS, Chem. Mater. 24 (2012) 4483–4490, https://doi.org/10.1021/cm300739y.

[42] A. Angel Ezhilarasi, J. Judith Vijaya, K. Kaviyarasu, L. John Kennedy, R. J. Ramalingam, H.A. Al-Lohedan, Green synthesis of NiO nanoparticles using Aegle marmelos leaf extract for the evaluation of in-vitro cytotoxicity, antibacterial and photocatalytic properties, J. Photochem. Photobio. B 180 (2018) 39–50, https://doi.org/10.1016/j.jphotobiol.2018.01.023.

[43] D. Sharma, J. Suriyaprakash, A. Dogra, S. Alijani, A. Villa, N. Gupta, Versatile carbon supported mono and bimetallic nanocomposites: synthesis, characterization and their potential application for furfural reduction, Mater. Today Chem. 17 (2020) 100319, https://doi.org/10.1016/j.mtchem.2020.100319.

[44] Y. Zhu, W. Zhao, J. Zhang, Z. An, X. Ma, Z. Zhang, Y. Jiang, L. Zheng, X. Shu, H. Song, X. Xiang, J. He, Selective activation of C-OH, C-O-C, or C=C in furfuryl alcohol by engineered Pt sites supported on layered double oxides, ACS Catal. 10 (2020) 8032–8041, https://doi.org/10.1021/acscatal.0c01276.

[45] C. Chen, R. Fan, W. Gong, H. Zhang, G. Wang, H. Zhao, The catalytic behaviour in aqueous-phase hydrogenation over a renewable Ni catalyst derived from a perovskite-type oxide, Dalton Trans. 47 (2018) 17276–17284, https://doi.org/10.1039/c8dt03907k.

[46] S.H. Pang, C.A. Schoenbaum, D.K. Schwartz, J.W. Medlin, Effects of thiol modifiers on the kinetics of furfural hydrogenation over Pd catalysts, ACS Catal. 4 (2014) 3123–3131, https://doi.org/10.1021/cs500598y.

[47] X. Di, C. Li, G. Lafaye, C. Especel, F. Epron, C. Liang, Influence of Re-M interactions in Re-M/C bimetallic catalysts prepared by a microwave-assisted thermolytic method on aqueous-phase hydrogenation of succinic acid, Catal. Sci. Technol. 7 (2017) 5212–5223, https://doi.org/10.1039/c7cy01039g.

[48] W. Liu, Y. Yang, L. Chen, E. Xu, J. Xu, S. Hong, X. Zhang, M. Wei, Atomically-ordered active sites in NiMo intermetallic compound toward low-pressure hydrodeoxygenation of furfural, Appl. Catal. B 282 (2021), 119569, https://doi.org/10.1016/j.apcatb.2020.119569.

[49] H. Yang, J.L. Whitten, Dissociative adsorption of H$_2$ on Ni(111), J. Chem. Phys. 98 (1993) 5039–5049, https://doi.org/10.1063/1.464958.

[50] Yanhui Yang, Sangyun Lim, Guoan Du, Chuan Wang, Dragos Ciuparu, Yuan Chen, aG.L. Haller, Controlling of physicochemical properties of nickel-substituted MCM-41 by adjustment of the synthesis solution pH and tetramethylammonium silicate concentration, J. Phys. Chem. B 110 (2006) 5927–5935, https://doi.org/10.1021/jp054255g.

[51] W. Ni, T. Wang, F. Heroguel, A. Krammer, S. Lee, L. Yao, A. Schuler, J. S. Luterbacher, Y. Yan, X. Hu, An efficient nickel hydrogen oxidation catalyst for hydroxide exchange membrane fuel cells, Nat. Mater. (2022) 1–7, https://doi.org/10.1038/s41563-022-01221-5.

[52] B.-W. Zhang, T. Zheng, Y.X. Wang, Y. Du, S.Q. Chu, Z. Xia, R. Amal, S.X. Dou, L. Dai, Highly efficient and selective electrocatalytic hydrogen peroxide production on Co-O-C active centers on graphene oxide, Commun. Chem. 5 (2022), 43, https://doi.org/10.1038/s42004-022-00645-z.

[53] F. Lan, H. Zhang, C. Zhao, Y. Shu, Q. Guan, W. Li, Copper clusters encapsulated in carbonaceous mesoporous silica nanospheres for the valorization of biomass-derived molecules, ACS Catal. 12 (2022) 5711–5725, https://doi.org/10.1021/acscatal.2c01270.

[54] S. Xiang, L. Dong, Z.Q. Wang, X. Han, L.L. Daemen, J. Li, Y. Cheng, Y. Guo, X. Liu, Y. Hu, A.J. Ramirez-Cuesta, S. Yang, X.Q. Gong, Y. Wang, A unique Co@CoO catalyst for hydrogenolysis of biomass-derived 5-hydroxymethylfurfural to 2,5-dimethylfuran, Nat. Commun. 13 (2022), 3657, https://doi.org/10.1038/s41467-022-31362-9.

[55] H. Zhao, W. Yin, M. Zhao, Y. Song, H. Yang, Hydrothermal fabrication and enhanced photocatalytic activity of hexagram shaped InOOH nanostructures with exposed {020} facets, Appl. Catal. B 130–131 (2013) 178–186, https://doi.org/10.1016/j.apcatb.2012.10.027.

[56] B. Liu, L. Wang, Y. Ma, Y. Yuan, J. Yang, M. Wang, J. Liu, X. Zhang, Y. Ren, Q. Du, H. Zhao, C. Pei, S. Liu, H. Yang, Enhanced gas-sensing properties and sensing mechanism of the foam structures assembled from NiO nanoflakes with exposed {1 1 1} facets, Appl. Surf. Sci. 470 (2019) 596–606, https://doi.org/10.1016/j.apsusc.2018.11.129.

[57] Y. Yang, L. Chen, Y. Chen, W. Liu, H. Feng, B. Wang, X. Zhang, M. Wei, The selective hydrogenation of furfural over intermetallic compounds with outstanding catalytic performance, Green Chem. 21 (2019) 5352–5362, https://doi.org/10.1039/c9gc01119f.

[58] S. Zhang, H. Xue, W.L. Li, J. Sun, N. Guo, T. Song, H. Dong, J. Zhang, X. Ge, W. Zhang, Q. Wang, Constructing precise coordination of nickel active sites on hierarchical porous carbon framework for superior oxygen reduction, Small (2021), e2102125, https://doi.org/10.1002/smll.202102125.

[59] Z. Chen, Y. Song, J. Cai, X. Zheng, D. Han, Y. Wu, Y. Zang, S. Niu, Y. Liu, J. Zhu, X. Liu, G. Wang, Tailoring the d-band centers enables Co$_4$N nanosheets to be highly active for hydrogen evolution catalysis, Angew. Chem. Int. Ed. Engl. 57 (2018) 5076–5080, https://doi.org/10.1002/anie.201801834.

[60] D. Luo, C. Li, Y. Zhang, Q. Ma, C. Ma, Y. Nie, M. Li, X. Weng, R. Huang, Y. Zhao, L. Shui, X. Wang, Z. Chen, Design of Quasi-MOF nanospheres as a dynamic electrocatalyst toward accelerated sulfur reduction reaction for high-performance lithium-sulfur batteries, Adv. Mater. 34 (2021), 2105541, https://doi.org/10.1002/adma.202105541.

[61] Y. Su, C. Chen, X. Zhu, Y. Zhang, W. Gong, H. Zhang, H. Zhao, G. Wang, Carbon-embedded Ni nanocatalysts derived from MOFs by a sacrificial template method for efficient hydrogenation of furfural to tetrahydrofurfuryl alcohol, Dalton Trans. 46 (2017) 6358–6365, https://doi.org/10.1039/c7dt00628d.

[62] C. Chen, C. Zhang, D. Zhao, S. Ding, C. Chen, The importance of constructing triple-functional Sr$_2$P$_2$O$_7$/Ni$_2$P catalysts for smoothing hydrogenation ring-rearrangement of biomass-derived furfural compounds in water, J. Catal. 421 (2023) 117–133, https://doi.org/10.1016/j.jcat.2023.03.007.